

Simulations of gravitational collapse in null coordinates IV: evolving through the event horizon, with an application to the spherical charged scalar field

Carsten Gundlach and Laetitia Martel

Mathematical Sciences, University of Southampton, Southampton SO17 1BJ, United Kingdom

(Dated: 18 November 2025, revised 9 January 2026)

We consider line elements of the form $-2G du (dx + B du) + R^2(...)$, where (...) does not contain dx . Surfaces of constant u are then null surfaces, and their affinely parameterised generators have tangent vector $G^{-1}\partial_x$. Considering u as the time coordinate, we can evolve either R or G , with the other one found by solving the Raychaudhuri equation along the null generators, or we can evolve both. This choice of *formulation* is independent from the remaining *gauge* choice $x \rightarrow x'(u, x, ...)$ in the line element above, which is fixed incrementally by the choice of B . For example, we can evolve G , in order to be able to evolve through an event horizon, and use B to adapt the coordinates to type-II critical collapse. As a demonstration of these ideas, we consider a charged scalar field in spherical symmetry. We consider two settings: a domain where the outgoing null cones emanate from a regular centre $R = 0$, and a domain where they emanate from an ingoing-null boundary. In both settings, we demonstrate convergence with resolution, within each formulation and between the three formulations. As testbeds, we compute the critical exponents and periodic fine-structures of the black hole charge and mass scaling laws in a one-parameter family of charged regular initial data, and examples of perturbed extremal Reissner-Nordström solutions.

CONTENTS

I. Introduction	1	D. Schwarzschild and extremal Reissner-Nordström	17
A. Overview	1	E. Perturbed extremal Reissner-Nordström	17
B. The problem posed by evolving through an event horizon in null coordinates	2	VII. Conclusions	18
C. Formulations and radial gauges in null coordinates	2	A. The Reissner-Nordström metric in null coordinates	19
D. Plan of this paper	4	B. Regular centre	20
II. The Einstein-Maxwell-charged scalar system	4	C. Expansions at the centre	20
A. Field equations in covariant form	4	D. Radial null geodesics peeling off the horizon	21
B. Field equations in spherical symmetry in null coordinates	5	E. Boundary conditions on an ingoing null cone intersecting an outgoing one	21
III. Algorithm	7	F. Discretization of the left boundary equations	22
A. Initial data and gauge choice	7	G. Convergence testing	22
B. Boundary conditions at $x = 0$	7	References	22
C. Time evolution algorithm	8		
IV. Numerical methods	8		
A. Discretization	8	I. INTRODUCTION	
B. Quantities that scale as a power of x at the centre	9		
C. Choice of time step	9	A. Overview	
D. Singularity excision	10		
V. Tests with a regular centre	10	In this series of papers, starting with [1], we have been developing numerical simulations of gravitational collapse on null cones emanating from a regular centre. Null coordinates are an established tool in spherical symmetry, but our main motivation is simulating critical collapse on null cones beyond spherical symmetry. As long as no caustics form, null coordinates are ideal for type-II critical collapse because they allow us to adapt the coordinate system to the approximate self-similarity and large range of scales seen there.	
A. Charged initial data	10		
B. Convergence tests	10	In the present paper, we introduce new formulations of the Einstein equations in null coordinates that allow	
C. Evolving through the event horizon and singularity excision	12		
D. Type-II critical collapse of a spherical charged scalar field	12		
E. The effect of charge on the critical scaling	13		
F. The role of the collapse criterion	14		
VI. Tests on a null rectangle	15		
A. Previous work	15		
B. Physical setup	16		
C. Prompt collapse	16		

us to evolve from regular data through the black hole event horizon, while keeping the radial coordinate arbitrary. The motivation for this will be given in more detail in the next Subsection, but, in brief, we want to evolve through horizons to accurately characterise black holes, while we also want to keep the radial coordinate arbitrary in order to adapt the coordinates to type-II critical collapse.

To make the presentation more concrete, after this Introduction we apply the new formulations to the spherical Einstein-Maxwell-charged scalar field system. After demonstrating convergence, we turn to type-II critical collapse in this system, and obtain some new physics results. In particular, we verify the critical exponents for the black hole mass and charge, calculate the mass and charge fine structures, and present preliminary evidence that the charge fine structure is not universal. We plan to return to non-spherical type-II critical collapse elsewhere.

The spherical Einstein-Maxwell-charged scalar systems is of current interest also because of the stable extremal critical collapse conjecture of Kehle and Unger [2, 3]. This says that there is an open region of solution space in which the threshold of black hole formation consists of extremal black holes.

In this context, we will need to evolve initial data posed on an outgoing and an ingoing null cone that meet at 2-sphere. The domain of dependence of these data is then a “null rectangle” in the symmetry-reduced spacetime. We present an algorithm for this setup, and demonstrate convergence in selected example solutions. We plan to investigate extremal critical collapse in this system elsewhere.

B. The problem posed by evolving through an event horizon in null coordinates

In Paper II of the series [4], we investigated the threshold of black hole formation for a massless scalar field coupled to general relativity in axisymmetry, adapting the coordinates to the expected self-similar critical solution. While, at moderate non-sphericity, this allowed us to fine-tune to the threshold of black hole formation down to machine precision, without any need for adaptive mesh-refinement, we could not reach non-sphericities as high as others had reached before us. In hindsight, this was due both to our choice of radial gauge (how the radial coordinate x labels points on each null cone generator) and our choice of formulation (which of the Einstein equations are used in the code and which are not). For our notation for the metric, see already Eq. (1) below.

Our *gauge* choice in Paper II was to make the area radius R a function $R(u, x)$ of retarded time u and radial coordinate x only, but not the two angular coordinates: we called this local shifted Bondi (lsB) gauge, as it is a generalisation of Bondi gauge $R = x$. We noted that near the event horizon, in highly non-spherical spacetimes, this was not a good gauge choice, as it caused the radial shift B required to keep R independent of the angles to diverge.

Separately, we chose the *formulation* where the met-

ric coefficient G is obtained by solving the Raychaudhuri equation along each outgoing null coordinate line. This formulation requires the area radius R to be strictly increasing along each null cone generator, that is $R_{,x} > 0$. In spherical symmetry, this still allows our time slices (outgoing null cones) to approach the event horizon asymptotically. Beyond spherical symmetry, there will be retarded times u_0 and u_1 such that the full event horizon is seen only after $u = u_1$, but in a formulation that requires $R_{,x} > 0$ the code must stop already at $u = u_0$.

The combination of lsB gauge and the formulation where G is constrained meant in practice that the simulations of highly non-spherical spacetimes near the black-hole threshold had to stop before they could be classified as either collapsing or dispersing.

This paper presents a second formulation, where the Raychaudhuri equation is solved for R , rather than for G . In the literature, this approach has been used only together with the affine radial gauge $G = 1$. Here we evolve G , which allows us to use an arbitrary radial shift B , and in particular one adapted to critical collapse.

We also present a third formulation, where both R and G are evolved and the Raychaudhuri equation is used only to construct initial data. In the literature, this formulation has been used only with double null gauge $B = 0$, but B can in fact be chosen freely.

One of our main points is the observation that all three formulations can be combined with any radial gauge choice.

The gauge problem in critical collapse mentioned above does not arise in spherical symmetry, and will be addressed when we return to axisymmetry elsewhere.

C. Formulations and radial gauges in null coordinates

We now give a more precise statement of what we just said about formulations. For clarity, we do not fix the spacetime dimension or symmetry. (In the remainder of the paper, we will restrict to spherical symmetry in 3+1 dimensions.) We consider line elements of the form

$$ds^2 = -2G du (dx + B du) + R^2 \gamma_{ij} (d\theta^i + \beta^i du) (d\theta^j + \beta^j du). \quad (1)$$

(The quantity B replaces the metric coefficient $H := -g_{uu}$ that we used in Papers I–III, with $B := H/(2G)$. This is just for convenience of notation.) The spacetime dimension is $n + 2$, and the θ^i are coordinates on an n -dimensional manifold, typically S^n . From this form of $g_{\mu\nu}$ it follows that $g^{uu} = g^{ui} = 0$, and $g^{ux} = -G^{-1}$. Hence the surfaces of constant u are null surfaces, and their affinely parameterised generators have tangent vector

$$U^a := -\nabla^a u = G^{-1} (\partial_x)^a. \quad (2)$$

We must have $G > 0$ for the metric to be regular. R is defined by restricting γ_{ij} to have a fixed determinant

(such as its value on a unit sphere S^n in standard coordinate θ^i). The remaining gauge freedom in this ansatz for the line element is to re-label u as $u \rightarrow u'(u)$, and to relabel the radial coordinate x as $x \rightarrow x'(u, x, \theta^i)$. We call a choice of coordinate x a radial gauge.

The expansion of the congruence of null generators can be expressed in terms of R as

$$\rho_+ = \frac{d \ln R}{d \lambda}, \quad (3)$$

where we have defined

$$\frac{d}{d \lambda} := G^{-1} \partial_x. \quad (4)$$

(See also Paper I [1] for the definition of ρ_+ from first principles.) The quantity

$$\lambda(u, x, \theta^i) := \int_0^x G(u, x', \theta^i) dx' \quad (5)$$

is a preferred affine parameter along the null generators. (We shall refer to it as “the” affine parameter).

The xx -component of the trace-reversed Einstein equations can be written as

$$R_{,xx} - \frac{G_{,x}}{G} R_{,x} + KR = 0, \quad (6)$$

or as

$$\left(\ln \frac{G}{R_{,x}} \right)_{,x} = \frac{KR}{R_{,x}}, \quad (7)$$

or as

$$\frac{d^2 R}{d \lambda^2} + \frac{K}{G^2} R = 0, \quad (8)$$

or as the Raychaudhuri equation

$$\frac{d \rho_+}{d \lambda} = -\rho_+^2 - \frac{K}{G^2}, \quad (9)$$

where the term K contains shear and matter terms, and is non-negative in vacuum or with matter obeying the dominant energy condition.

From (8), with $K \geq 0$, we see that once $dR/d\lambda$ has become negative, R reaches zero in finite affine parameter. Equivalently, from (9) we see that once ρ_+ has become negative, it blows up in finite affine parameter. We can now make the above statement precise: In a non-spherical collapse spacetime, generically there will be $u_0 < u_1$ such that for any coordinate null cone with $u_0 < u < u_1$, the expansion ρ_+ remains positive on some of its generators, while on others it becomes negative and then blows up. This could be because the generator has reached a curvature singularity, or because the null cone has developed a caustic.

We now come to the role of the Raychaudhuri equation in numerical relativity on null cones. In its form (6) and with G given, it can be solved as a second-order ordinary differential equation (from now on, ODE) in x for R . In its form (7) and with R given, it can be solved as a first-order ODE for G . We also have wave equation-like evolution equations $G_{,ux} = \dots$ and $R_{,ux} = \dots$ for both G and R . This gives rise to three formulations, each of which admits an arbitrary radial gauge:

- evolve R and constrain G (**evolve- R formulation**, from now on **eR**);
- evolve G and constrain R (**evolve- G formulation**, from now on **eG**);
- evolve R and G freely and impose the constraint between them only at $u = 0$ (**free-evolution formulation**, from now on **fe**).

The eR formulation requires $R_{,x} > 0$, because we divide by $R_{,x}$ in (7), and so it breaks down once any part of a coordinate null cone intersects the black hole region. The other two formulations allow us to evolve further. It is this observation that motivates us to consider eG and fe in the present paper.

After the radial gauge has been fixed in the initial data at $u = 0$, typically by specifying either R or G as a function of (x, θ^i) , it is controlled *incrementally* by the choice of the quantity B . The prototype incremental gauge choice is double-null gauge $B = 0$, which makes x an ingoing null coordinate.

In addition to the three formulations above, there are two particular *combinations* of formulation and gauge that remove the need for one evolution equation, and which we feel should be characterised as formulations:

- set $R = x$ and constrain G (**Bondi formulation**);
- set $G = 1$ and constrain R (**affine formulation**).

In both these formulations, all time evolution equations (equations containing u -derivatives) correspond to physical (matter and gravitational wave) degrees of freedom, so they are “maximally constrained” in the language of numerical relativity. By contrast, eR and eG have one gauge evolution equation, and fe has two. Table I summarises the five formulations we have just discussed. The observation that the choices of formulation and gauge are independent is one of the main points of the present paper.

One can retain some of the stability advantages of a maximally constrained formulation in the eR formulation by restricting to the family of “local shifted Bondi” (lsB) radial gauges, where $R = R(u, x)$. We did this in Paper II. Similarly, in the eG formulation, we can restrict to “local shifted affine” (lsa) gauges, where $G = G(u, x)$, to make it almost maximally constrained.

We are aware of the following combinations of formulation and gauge choice used for numerical time evolution in the literature. We hope that the list of such combinations is complete, but the list of references is only intended to be indicative:

- double-null gauge in fe formulation, in spherical symmetry: applied to critical collapse [5], and to black hole interiors [6–8];
- double-null gauge in eR formulation, in spherical symmetry: applied to critical collapse [9, 10];

Formulation	Initial gauge	Evolved gauge	Restricted to	Gauge evolution equations
Bondi	$R = x$	$R = x$	$R_{,x} > 0$	0
affine	$G = 1$	$G = 1$	—	0
eR	any R or G	any B	$R_{,x} > 0$	1
eG	any R or G	any B	—	1
free evolution	any R or G	any B	—	2

TABLE I. Summary of the five formulations discussed in Sec. IC. “Initial gauge” denotes the freedom to label points on $u = 0$ by the coordinate x , so “any R ” is short for “any choice of $R(0, x, \theta^i)$ ” and similarly for “any G ”. “Evolved gauge” denotes how the coordinate x is propagated to $u > 0$, and “any B ” is short for “any choice of $B(u, x, \theta^i)$ ”. The restriction to $R_{,x} > 0$ arises when the Raychaudhuri equation is solved for G given R , and means that we cannot evolve through an event horizon. We have suppressed the function arguments in the table so that it applies for any spatial symmetry or none, and any spacetime dimension. “Gauge evolution equations” denotes the number of equations containing u -derivatives in the formulation, minus the number of physical degrees of freedom (where in the absence of symmetry we count vacuum gravity as two degrees of freedom, a scalar field as one, etc).

- Bondi formulation, in spherical symmetry: applied to critical collapse [11–14], and to black-hole interiors, [15];
- Bondi formulation, beyond spherical symmetry: applied to axisymmetric weak fields [16], and to gravitational wave extraction [17], see also [18];
- affine formulation, in spherical symmetry: applied to critical collapse [19], see also [20];
- affine formulation, in planar symmetry: applied to asymptotically anti-de Sitter spacetimes [21];
- affine formulation, beyond spherical symmetry: applied to asymptotically anti-de Sitter spacetimes [22–24], see also [25].

In our own previous work, we have explored the following additional combinations:

- “shifted double null” gauge in eR formulation, in spherical symmetry: applied to critical collapse [26], see also [1];
- “local shifted Bondi” gauge in eR formulation, in axisymmetry: applied to critical collapse [4], see also [1].

D. Plan of this paper

In the remainder of this paper, we will restrict to spherical symmetry in 3+1 dimensions, with charged scalar field matter, but the ideas illustrated here are in principle easily generalised to less symmetry, other spacetime dimensions, and to vacuum or other matter.

We present an implementation of the five formulations described above in one code, and we test the three formulations that admit a general radial gauge in two settings. In the first of these, we evolve on outgoing null cones that emanate from a regular central worldline. To fix the radial gauge in the initial data, we either set $R = x$ or $G = 1$ at $u = 0$. We continue in “shifted double-null gauge”, see Eq. (60) below, an incremental gauge that is adapted to critical collapse in spherical symmetry (see also Sec. III.C of Paper I for a definition and [26] for a previous application). As a

physics application, we compute the fine-structure of the mass and charge scaling laws in critical collapse, which has not been computed before. In the second setting the left boundary $x = 0$ is not a regular centre but an ingoing null cone, so that the computational domain is a null rectangle. We continue the initial gauge choice of $R_{,x} = 1$ or $G = 1$ as double-null gauge $B = 0$.

We do not present any results in the affine and Bondi formulations, as the affine and Bondi gauges that they require do not allow us to make the outer boundary future spacelike (in the first setting) or ingoing null (in the second setting).

In both settings, we present evidence of second-order convergence with resolution, both within each formulation and between the three pairs of formulations. With a regular centre, the convergence is not quite pointwise at the first few grid points, but it is pointwise elsewhere, and is second-order in any norm. By contrast, on the null rectangle, where we do not need an expansion, the convergence is cleanly pointwise.

We devise a simple singularity excision scheme, and present evidence that it works in the eG and free evolution formulations (eR cannot evolve through the apparent horizon).

In Sec. II we give the field equations for the spherical Einstein-charged-scalar system, in Sec. III we present our solution algorithm, and in Sec. IV our numerical methods. Sec. V presents tests on a domain with a regular centre, including convergence tests, critical collapse, and singularity excision, and Sec. VI presents tests on a null rectangle domain, including convergence tests, collapse, and singularity excision. We conclude in Sec. VII.

II. THE EINSTEIN-MAXWELL-CHARGED SCALAR SYSTEM

A. Field equations in covariant form

The matter is a complex scalar $\phi =: \psi + i\chi$ field coupled to electromagnetism. The action, in units where

$c = G_N = 1$, is

$$S = \int \left(\frac{R}{16\pi} - \frac{1}{2} D_a \phi (D^a \phi)^* - \frac{1}{16\pi} F_{ab} F^{ab} \right) \sqrt{-g} d^4 x, \quad (10)$$

where a star denotes the complex conjugate, the field strength tensor F in terms of the potential A is

$$F_{ab} := \nabla_a A_b - \nabla_b A_a, \quad (11)$$

and we have introduced the charge-covariant derivative

$$D_a := \nabla_a + iqA_a. \quad (12)$$

Our electromagnetic convention is similar to Gauss units, and our scalar field convention reduces to the standard one for a real scalar field ψ if $\chi = 0$. These are also the conventions of [13]. The convention of [31] differs by the absence of the factor $1/2$ in the scalar field term. The convention of [8] differs by factors of 16π in front of R and 4π in front of $F_{ab} F^{ab}$.

ϕ obeys the wave equation

$$D^a D_a \phi = 0. \quad (13)$$

The Maxwell equations are

$$\nabla_b F^{ab} = 4\pi j^a, \quad (14)$$

where the charge current is

$$j_a = -\frac{iq}{2} (D_a \phi)^* \phi + c.c. \quad (15)$$

$$= q(\chi \nabla_a \psi - \psi \nabla_a \chi) - q^2 A_a (\psi^2 + \chi^2). \quad (16)$$

It is conserved, $\nabla_a j^a = 0$, because F^{ab} is antisymmetric. The trace-reversed Einstein equations are

$$E_{ab} := R_{ab} - 8\pi S_{ab} = 0, \quad (17)$$

where the trace-reversed stress-energy tensor is

$$S_{ab} = \frac{1}{2} (D_a \phi (D_b \phi)^* + (D_a \phi)^* D_b \phi) + \frac{1}{4\pi} \left(F_{ac} F_b^c - \frac{1}{4} g_{ab} F_{cd} F^{cd} \right). \quad (18)$$

The equations admit the gauge freedom $\phi \rightarrow e^{iq\alpha} \phi$, $A_a \rightarrow A_a + \nabla_a \alpha$ for an arbitrary scalar function α , leaving F_{ab} and $D_a \phi$, and hence j^a and T_{ab} , invariant.

B. Field equations in spherical symmetry in null coordinates

We consider the general metric in spherical symmetry with one null coordinate u ,

$$ds^2 = -2G du(dx + B du) + R^2 d\Omega^2, \quad (19)$$

where G , B and R are functions of (u, x) , and $d\Omega^2 := d\theta^2 + \sin^2 \theta d\varphi^2$. The surfaces of constant u are outgoing null cones. The choice of coordinate x along the null cone generators (the radial gauge) is not yet fixed.

Starting from an arbitrary electromagnetic gauge, the particular gauge

$$A_x(u, x) = 0, \quad A_u(u, 0) = 0 \quad (20)$$

can be achieved by the gauge transformation with

$$\alpha(u, x) = - \int_0^u A_u(u', 0) du' - \int_0^x A_x(u, x') dx'. \quad (21)$$

From now on, we work exclusively in this gauge, and for conciseness we rename A_u to A . Note that $A_x = 0$ can be written geometrically as $U^a A_a = 0$.

We define the ingoing null vector field

$$\Xi := \partial_u - B \partial_x, \quad (22)$$

which is normalised relatively to U^a as $U^a \Xi_a = -1$. For the scalar field, we also introduce

$$\hat{\Xi} \phi := (\Xi + iqA) \phi, \quad (23)$$

with real and imaginary parts

$$\hat{\Xi} \psi := \text{Re } \hat{\Xi} \phi = \Xi \psi - qA \chi, \quad (24)$$

$$\hat{\Xi} \chi := \text{Im } \hat{\Xi} \phi = \Xi \chi + qA \psi. \quad (25)$$

The two components of the Maxwell equations can be written in terms of the local charge function

$$Q := \frac{R^2 A_{,x}}{G}. \quad (26)$$

The Maxwell equations become

$$Q_{,x} = 4\pi q R^2 (\psi \chi_{,x} - \chi \psi_{,x}), \quad (27)$$

$$\Xi Q = 4\pi q R^2 (\chi \hat{\Xi} \psi - \psi \hat{\Xi} \chi). \quad (28)$$

Hence we have a conserved charge current $\nabla_a j^a = 0$ with

$$j^u = \frac{1}{4\pi G R^2} Q_{,x}, \quad j^x = -\frac{1}{4\pi G R^2} Q_{,u}, \quad (29)$$

where an overall constant has been fixed from (14), and we have used $\sqrt{-g} = GR^2 \sin \theta$.

We can write the Einstein and Maxwell equations in terms of Ξ , $\hat{\Xi}$ and Q , without any explicit appearance of A , B and ∂_u , with the exception of the Einstein equation E_{ux} . However, we still need to find B in order to recover ∂_u from Ξ , and we need to find A to recover Ξ from $\hat{\Xi}$. We find A by integrating (26), written as

$$A_{,x} = \frac{GQ}{R^2}. \quad (30)$$

In spherical symmetry, the Hawking mass M of a symmetry sphere is a scalar on the reduced spacetime, and is then also called the Misner-Sharp mass, or the Kodama mass. It is given by

$$M := \frac{CR}{2}, \quad (31)$$

where we define the Hawking compactness C of a symmetry sphere (equivalent to a point in the reduced spacetime) as

$$C := 1 - |\nabla R|^2. \quad (32)$$

In our coordinates, C is given by

$$C(u, x) = 1 + \frac{2R_{,x}\Xi R}{G}. \quad (33)$$

The derivatives of the Misner-Sharp mass are

$$M_{,x} = -4\pi \frac{R^2 \Xi R}{G} (\psi_{,x}^2 + \chi_{,x}^2) + \frac{Q^2 R_{,x}}{2R^2}, \quad (34)$$

$$\Xi M = -4\pi \frac{R^2 R_{,x}}{G} (\hat{\Xi}\psi^2 + \hat{\Xi}\chi^2) + \frac{Q^2 \Xi R}{2R^2}. \quad (35)$$

Hence there is a conserved mass current analogous to (29).

We also define the augmented mass

$$\mathcal{M} := M + \frac{Q^2}{2R}. \quad (36)$$

(Other authors call it the renormalised mass.) As Q and M are scalars on the reduced spacetime, so is \mathcal{M} . Its derivatives are

$$\begin{aligned} \mathcal{M}_{,x} &= -4\pi \frac{R^2 \Xi R}{G} (\psi_{,x}^2 + \chi_{,x}^2) \\ &\quad + 4\pi qQR(\psi\chi_{,x} - \chi\psi_{,x}), \end{aligned} \quad (37)$$

$$\begin{aligned} \Xi \mathcal{M} &= -4\pi \frac{R^2 R_{,x}}{G} (\hat{\Xi}\psi^2 + \hat{\Xi}\chi^2) \\ &\quad + 4\pi qQR(\chi\hat{\Xi}\psi - \psi\hat{\Xi}\chi). \end{aligned} \quad (38)$$

Hence there is another conserved mass current analogous to (29).

In electrovacuum, defined by $\phi = 0$ (in our electromagnetic gauge choice $A_x = 0$), both Q and \mathcal{M} are constant, and are equal to the parameters Q_0 and \mathcal{M}_0 of the Reissner-Nordström (from now on, RN) family of solutions (see Appendix A), while M is not constant unless $Q = 0$. On the other hand M is non-decreasing along outgoing null rays, in the sense that $R_{,x} > 0$ implies $M_{,x} \geq 0$, both in vacuum and for any matter obeying the dominant energy condition.

We note that M can be computed from R and ΞR via (31) and (32), or by integrating (34) from $M = 0$ at $R = 0$. Similarly, \mathcal{M} can be computed from M or by integrating (37) from $\mathcal{M} = 0$ at $R = 0$. We call these integrated versions of M and \mathcal{M} , \tilde{M} and $\tilde{\mathcal{M}}$. In the discretised equations, M differs from \tilde{M} , and \mathcal{M} from $\tilde{\mathcal{M}}$, but by construction \tilde{M} retains the non-decreasing property, and $\tilde{\mathcal{M}}$ the constant-in-electrovacuum property, even in the presence of numerical error.

In spherical symmetry, only the components E_{uu} , E_{ux} , E_{xx} and $E_+ := E_{\theta\theta} = E_{\varphi\varphi}/\sin^2\theta$ of the trace-reversed Einstein equations are algebraically independent. We can write $E_{xx} = 0$ as

$$\left(\ln \frac{G}{R_{,x}} \right)_{,x} = 4\pi \frac{R(\psi_{,x}^2 + \chi_{,x}^2)}{R_{,x}}, \quad (39)$$

which can be integrated for G , given R , ψ and χ , but only if $R_{,x} > 0$. Alternatively, we can write it as

$$R_{,xx} - \frac{G_{,x}}{G} R_{,x} + 4\pi(\psi_{,x}^2 + \chi_{,x}^2)R = 0, \quad (40)$$

which can be solved as a second-order linear ODE for R , given G , ψ and χ . There is then no restriction on the sign of $R_{,x}$. More geometrically, $E_{xx} = 0$ can be written as

$$UUR + 4\pi[(U\psi)^2 + (U\chi)^2]R = 0. \quad (41)$$

It is the Raychaudhuri equation for the generators of the coordinate null cones.

We can write $E_+ = 0$ and the real and imaginary parts of the complex wave equation as

$$(R\Xi R)_{,x} = -\frac{G}{2} \left(1 - \frac{Q^2}{R^2} \right), \quad (42)$$

$$(R\hat{\Xi}\psi)_{,x} = -(\Xi R)\psi_{,x} - \frac{qQG\chi}{2R}, \quad (43)$$

$$(R\hat{\Xi}\chi)_{,x} = -(\Xi R)\chi_{,x} + \frac{qQG\psi}{2R}. \quad (44)$$

$E_{ux} = 0$ can be written as

$$\begin{aligned} \mathcal{H}_{,x} &= -\frac{G + 2R_{,x}\Xi R}{R^2} + \frac{2GQ^2}{R^4} \\ &\quad + 8\pi(\chi_{,x}\hat{\Xi}\chi + \psi_{,x}\hat{\Xi}\psi) \end{aligned} \quad (45)$$

$$= -\frac{2G\mathcal{M}}{R^3} + \frac{3GQ^2}{R^4} + 8\pi(\dots), \quad (46)$$

where

$$\mathcal{H} := B_{,x} - \Xi \ln G \quad (47)$$

is the only place where B appears in the Einstein equations, other than in the combination Ξ . E_{ux} is a combination of derivatives of the other Einstein equations, and is therefore sometimes called the “redundant” equation, but in the eG and fe formulations we use it to obtain $\Xi \ln G$, given an arbitrary B , while in the affine formulation we use it to obtain B , given $G = 1$.

The case where $x = 0$ is a regular centre $R = 0$ is considered in Appendix B. From regularity, M , Q , \mathcal{M} , $R\Xi R$, $R\Xi\psi$ and $R\Xi\chi$ all vanish at $x = 0$, A vanishes there as an electromagnetic gauge choice, and \mathcal{H} vanishes because of regularity and because we choose u to be proper time at the centre. Hence we have trivial boundary conditions for the integration of all hierarchy equations.

The remaining Einstein equation $E_{uu} = 0$ can be written as

$$\Xi\Xi R + \mathcal{H}\Xi R + 4\pi R(\hat{\Xi}\psi^2 + \hat{\Xi}\chi^2) = 0. \quad (48)$$

It is the Raychaudhuri equation on the ingoing null geodesics. We do not use it in our time evolution scheme with a regular centre, but it acts as a constraint on the data we can impose on a left boundary that is ingoing null. In analogy to (41), we can write it more geometrically as

$$XXR + 4\pi[(\hat{X}\psi)^2 + (\hat{X}\chi)^2]R = 0, \quad (49)$$

where

$$X := \bar{G}^{-1}\Xi, \quad \hat{X} := \bar{G}^{-1}\hat{\Xi}. \quad (50)$$

X is tangent to the affinely parameterised ingoing null geodesics (as U is to the outgoing ones), and \bar{G} is defined by

$$\Xi \ln \bar{G} = -\mathcal{H}, \quad (51)$$

or equivalently by

$$\Xi \ln \left(\frac{\bar{G}}{G} \right) = -B_{,x}. \quad (52)$$

In double-null gauge $B = 0$, we have $\bar{G} = G$ and $X = G^{-1}\partial_u$, in analogy to $U = G^{-1}\partial_x$ (the latter holds in any radial gauge).

In initial data on an outgoing null cone with regular centre, we always choose $\Xi R < 0$ and hence $XR < 0$ on $u = 0$. From (49) we see that $XXR \leq 0$, so $XR < 0$ and hence $\Xi R < 0$ on the entire domain of dependence of these initial data. This is not obvious from (42), whose right-hand side becomes negative when $R < |Q|$, and so, as we solve (42) but not (49), $\Xi R < 0$ may be violated by numerical error.

As $R \geq 0$, $G > 0$ and $\Xi R < 0$, ρ_+ given above in (3) has the same sign as $R_{,x}$. Hence a symmetry sphere is outer-trapped if and only if $R_{,x} < 0$, or equivalently $C > 1$.

The choice of coordinate x for $u > 0$ is controlled incrementally by the choice of B . This plays a role similar to the radial shift vector component in the ADM formulation. To see this, note that if we make a transformation from double-null coordinates (u, v) to general null coordinates (u, x) , parameterised by $v = v(u, x)$, then

$$-2\bar{G}du\,dv = -2G\,du(dx + B\,du) \quad (53)$$

holds if and only if

$$G = \bar{G}v_{,x}, \quad (54)$$

$$v_{,u} = Bv_{,x}, \quad (55)$$

regardless of spacetime dimension or symmetry, and so v is advected in x with speed $-B$.

Our key diagnostics are the Hawking compactness C , Hawking mass M , charge Q and augmented mass \mathcal{M} defined above. Extending the definition in Paper II, we define

$$T := \max_{\text{whole spacetime}} |(D_a\phi)^* D^a \phi| \quad (56)$$

as an additional diagnostic. Note that $\max |R_a{}^a| = 8\pi T$. This gives us a curvature quantity that scales on the dispersion side of the collapse threshold.

III. ALGORITHM

s

A. Initial data and gauge choice

To set initial data, we specify $\psi(x)$ and $\chi(x)$ freely. We then either initialise $G = 1$ and solve (40) to initialise R , or we initialise $R = x$ and solve (39) to initialise G . These are physically inequivalent data for

the same functions $\psi(x)$ and $\chi(x)$, as they correspond to different geometrically defined data functions $\psi(R)$ and $\chi(R)$, or equivalently $\psi(\lambda)$ and $\chi(\lambda)$.

In Bondi gauge $R = x$, the identity $R_{,u} = 0$ determines B as

$$B_{\text{Bondi}} = -\frac{\Xi R}{R_{,x}}. \quad (57)$$

All our gauge choices keep $R = 0$ at $x = 0$, and so $R_{,u} = 0$ at the centre. With u defined to be proper time there, we have

$$B(u, 0) = B_{\text{Bondi}}(u, 0) = \frac{1}{2R_{,x}(u, 0)}, \quad (58)$$

see also Eq. (B7) below.

In affine gauge $G = 1$, the identity $\Xi G = 0$ determines B as

$$B_{\text{affine}} = B_{\text{Bondi}}(u, 0) + \int_0^x \mathcal{H} dx', \quad (59)$$

where we have used (58).

For critical collapse in spherical symmetry, we use a radial gauge where B is a linear function of x , fixed to coincide with Bondi gauge at $x = 0$ (so that $R = 0$ remains at $x = 0$) and to vanish at $x = x_0$ (so that $x = x_0$ is an ingoing null cone). This gives

$$B_{\text{sdn}}(u, x) = B_{\text{Bondi}}(u, 0) \left(1 - \frac{x}{x_0} \right). \quad (60)$$

It is easy to see from (55) that if $v = x$ on $u = 0$ and B is proportional to x , then v remains linear in x , with $v = x_0$ at $x = x_0$ and $R = 0$ at $x = 0$, for all $u \geq 0$. This simple linear relation between v and x motivates the name ‘shifted double-null’ (sdn) gauge.

B. Boundary conditions at $x = 0$

When $x = 0$ is the regular central worldline $R = 0$, $x = 0$ is a coordinate singularity, and we cannot impose simple boundary conditions there. To start up the integration of the hierarchy equations, we expand in powers of x instead.

At a given u , we fit the evolved quantities ψ , χ , R/x and/or G either to linear functions of x , such as $\psi \simeq \psi_{(0)} + \psi_{(1)}x$, or to quadratic ones, such as $\psi \simeq \psi_{(0)} + \psi_{(1)}x + \psi_{(2)}x^2$. (The notation here is compatible with our notation $\psi_{l(n)}$ in Papers I and II, where l denotes the spherical harmonic and n the power of x .)

$R_{(1)}$, $G_{(0)}$ and $\mathcal{H}_{(0)}$ are not determined by the equations. However, we show in Appendix B that at a regular centre, and with u proper time at the centre, they obey $G_{(0)} = R_{(1)}$, $B_{(0)} = 1/(2R_{(1)})$ and $\mathcal{H}_{(0)} = 0$.

The full expressions for the expansion coefficients are given in Appendix C.

On the other hand, if $x = 0$ is a timelike or null boundary, we can specify boundary conditions for the hierarchy equations there, subject to constraints. For the case where $x = 0$ is an ingoing null cone, we discuss this in detail in Appendix E.

C. Time evolution algorithm

We use the ‘‘method of lines’’ framework, where one discretises separately in space and time. We break up each sub-timestep into the following steps, where Steps 1 and 3 depend on the formulation. For completeness, we include the affine and Bondi formulations in the following pseudo-code, even though we do not use them for any numerical tests in this paper.

Step 0: Assume that on a null cone of constant u , the functions $\psi(x)$, $\chi(x)$, and $G(x)$ and/or $R(x)$ are given. When G and R are both given, they must obey the constraint (40). With a regular centre, we fit these functions to power-series expansions in x about $x = 0$.

Step 1a: In the eR or Bondi formulation, we solve the Raychaudhuri equation in its form (39) for G by integration, and set the fitting coefficients of G consistently.

Step 1b: Alternatively, in the eG or affine formulation, we solve the Raychaudhuri equation in its form (40) as a homogeneous linear second-order ODE for R , and we set the fitting coefficients of R consistently.

Step 1c: Alternatively, in the fe formulation we do nothing. From numerical error, both in the evolution of R and G , and in the fitting, the fitting coefficients of R and G will not be exactly compatible with the Raychaudhuri equation, so we need to make an arbitrary choice which set of fitting coefficients we choose for expanding the solution of the hierarchy equations at the centre. The choice made in Appendix C works.

Step 2: We now solve (27) for Q and then (30) for A by integration. Next we solve (42) for ΞR by integration, followed by (43) and (44) for $\hat{\Xi}\psi$ and $\hat{\Xi}\chi$, and hence $\Xi\psi$ and $\Xi\chi$. Finally, we solve (37) for \mathcal{M} (which, obtained thus, we call $\hat{\mathcal{M}}$) and then (46) for \mathcal{H} . (In the eR and Bondi formulations, \mathcal{H} is not required, and we compute it only as a diagnostic.)

Step 3a: In the affine formulation, we compute B from (59).

Step 3b: Alternatively, in the Bondi formulation, B is given explicitly by (57).

Step 3c: Alternatively, in the eR, eG and fe formulations we set B freely. For critical collapse in spherical symmetry, we use sdn gauge (60). On a null rectangle we use double-null gauge $B = 0$.

Step 4: We find the u -derivatives of ψ , χ , R and/or $\ln G$ from their Ξ -derivatives and x -derivatives, using (22). The x -derivatives are upwinded depending on the sign of B . At $x = 0$ this makes the upwind derivative a right derivative, and at $x_{\max} > x_0$ a left derivative.

Step 5: Using an ODE integrator at each grid point (the method of lines), we evolve ψ , χ , and one or both of R and $\ln G$, from u to $u + \Delta u$. This returns us to Step 0.

IV. NUMERICAL METHODS

A. Discretization

With $x = R = 0$ a regular centre, we use an equally spaced centered grid $x_i = i\Delta x$, $i = 1 \dots N_x$, so that $x = 0$ is not on the grid. With $x = 0$ an ingoing null cone, we use $x_i = i\Delta x$, $i = 0, 1 \dots N_x$.

The ODEs in x can be solved by integration using an integrating factor. They can therefore be written as $g_{,x} = F(f, f_{,x})$, where the f are already known and g is to be determined. We use the explicit integration scheme

$$g_i \simeq g_{i-1} + F\left(f_{i-\frac{1}{2}}, (f_{,x})_{i-\frac{1}{2}}\right) \Delta x, \quad (61)$$

with

$$f_{i-\frac{1}{2}} \simeq \frac{f_i + f_{i-1}}{2}, \quad (62)$$

$$(f_{,x})_{i-\frac{1}{2}} \simeq \frac{f_i - f_{i-1}}{\Delta x}. \quad (63)$$

This scheme is explicit, is second-order accurate by construction, and is causal in the sense that the vector of variables g_i depends only on g_j with $j < i$ and f_j with $j \leq i$: information propagates along a null cone of constant u only towards increasing x .

To solve the Raychaudhuri equation (40) for R , we write it in the first-order form

$$R_{,x} = GV, \quad (64)$$

$$V_{,x} = -\frac{K}{G}R, \quad (65)$$

with

$$V := \frac{R_{,x}}{G}, \quad (66)$$

$$K := 4\pi(\psi_{,x}^2 + \chi_{,x}^2). \quad (67)$$

When we solve (65,64) for (V, R) , the coefficients G and K are already known.

K is naturally given at midpoints, but G needs to be interpolated there using (62). We discretize this system, using a 2-point stencil, to second-order accuracy as

$$\frac{R_i - R_{i-1}}{\Delta x} = G_{i-\frac{1}{2}} \frac{V_i + V_{i-1}}{2}, \quad (68)$$

$$\frac{V_i - V_{i-1}}{\Delta x} = -\frac{K_{i-\frac{1}{2}}}{G_{i-\frac{1}{2}}} \frac{R_i + R_{i-1}}{2}. \quad (69)$$

This can be solved for R_i and V_i , giving us the explicit scheme

$$\begin{pmatrix} R_i \\ V_i \end{pmatrix} = \frac{1}{1 + \mathcal{K}} \begin{pmatrix} 1 - \mathcal{K} & \mathcal{G} \\ -\frac{4\mathcal{K}}{\mathcal{G}} & 1 - \mathcal{K} \end{pmatrix} \begin{pmatrix} R_{i-1} \\ V_{i-1} \end{pmatrix}, \quad (70)$$

where

$$\mathcal{K} := K_{i-\frac{1}{2}} \frac{\Delta x^2}{4}, \quad (71)$$

$$\mathcal{G} := G_{i-\frac{1}{2}} \Delta x. \quad (72)$$

The two complex eigenvalues of this linear map have absolute value 1 for any $\mathcal{K} \geq 0$, so that the method is unconditionally stable. The method is exact for $K = 0$. It has no amplitude error when $K_{,x} = G_{,x} = 0$, in the sense that then $(KR^2 + G^2V^2)_{,x} = 0$ in the discretisation, as it is in the continuum.

$V(x)$ changes sign at most once (from positive to negative) over the x -domain. This means that $K \lesssim x_{\max}^{-2}$, and so $\mathcal{K} \lesssim N_x^{-2} \ll 1$. Hence we can expect the numerical error to be reasonably small.

For comparison, we also use the second or fourth-order Adams-Bashforth method. These need the vector of right-hand sides F_i at grid points. We discretize x -derivatives on grid points as

$$(f_{,x})_i \simeq \frac{f_{i+1} - f_{i-1}}{2\Delta x} \quad (73)$$

where this is defined, and the standard one-sided three-point stencils at the left and right boundaries $i = 1$ and $i = N_x$. This is also second-order accurate but not causal.

When we solve (39) for G , we first find $-\ln V$ on grid points by integration, where $V := R_{,x}/G$. (In Papers I-III, we used the variables $g := 1/V$ and $\gamma := \ln g$. We have replaced them with V as they are defined only for $R_{,x} > 0$.) We then find V at grid points and hence at mid-points, and hence $G = R_{,x}/V$ at mid-points in a causal and second-order accurate way, given that $R_{,x}$ is known to second order and causally at mid-points.

We linearly interpolate G from the mid-points to grid points (and we linearly extrapolate to the grid points $i = 1$ and $i = N_x$). This is second-order accurate but with an additional error from the interpolation, and it is no longer causal. However, we need G at grid points only for output and to initialise $\ln G$ from initial data in Bondi gauge. The non-causality does not matter for output and initialisation. To evaluate the compactness C when G is constrained, we use V on grid points.

G varies rapidly in u and x , but is constrained to be strictly positive. To avoid it becoming negative through numerical error, we evolve $\ln G$ rather than G . We find G at grid points by exponentiating, and hence on mid-points by linear interpolation. To evaluate the compactness C when G is evolved, we use $R_{,x}$ on gridpoints, which is not causal. Again we do not see an adverse effect.

In the evolution equations

$$f_{,u} = \Xi f + B f_{,x} \quad (74)$$

where f stands for ψ , χ , R and $\ln G$, we discretize the transport term $f_{,x}$ by second-order upwinding, depending on the sign of B . If our solution method for the hierarchy equations is also causal, as defined above, our complete numerical method is strictly causal, in the sense that all grid points are computed only from grid points in their causal past. In particular, with $B < 0$ at $i = N_x$ and $i = N_x - 1$, the outer boundary is treated numerically like any other point.

In any gauge where $R = x$ stays at $x = 0$ we need to evaluate $R_{,x}$ at the centre to impose (58). Given that the upwinded transport term $BR_{,x}$ should cancel

ΞR to give us $R_{,u} = 0$ at the centre, we compute $R_{,x}$ at the centre as the second-order upwind derivative

$$R_{(1)} := R_{,x}(u, 0) \simeq \frac{2R_1 - \frac{1}{2}R_2}{\Delta x}. \quad (75)$$

Other choices result in an instability at the centre.

We solve the $f_{,u} = F[f]$ evolution equations using a Runge-Kutta ODE solver (typically second-order) in u , and we solve the ODEs in x that give $F[f]$ at each sub-timestep.

B. Quantities that scale as a power of x at the centre

The quantity Q is obtained by integration of (27). From its definition, the quantity Q/R^3 , representing an average charge density, is expected to be smooth, and to be non-zero at the centre. Numerically, this smoothness is not guaranteed. We can improve regularity by discretizing

$$\int_{x_{i-1}}^{x_i} f R^2 dx \simeq \frac{1 - \epsilon + \frac{\epsilon^2}{3}}{1 - \epsilon + \frac{\epsilon^2}{4}} f_{i-1/2} (R_{i-1/2})^2 \Delta x, \quad (76)$$

where $\epsilon := 1/i$. This is exact when R/x and f are constant. Applying this to the computation of Q does not make a big difference for Q itself, but it does for A , which is the integral of Q/R^2 . We apply the same correction factor in the integral for \tilde{M} , to correct for a naive midpoint value of $Q/R \sim x^2$.

For a similar reason, wherever we need to evaluate M/R^3 , Q/R^2 and similar quantities, in the mid-point rule we take the average of M/R^3 at x_i and x_{i-1} , rather than averaging M and R .

Finally, a more accurate way of evaluating (45) is to rewrite it as (46), and then evaluate \mathcal{M} in the first term as \tilde{M} , the integral expression for \mathcal{M} . We find heuristically that this is essential for \mathcal{H} and hence $\Xi \ln G$ to converge with resolution.

C. Choice of time step

In the spherical and axisymmetric scalar critical collapse simulations of Paper II we used the timestep $\Delta u = \Delta u_1$, where

$$\Delta u_1 := C_1 \min_x \left| \frac{R_{,x}}{\Xi R} \right| \Delta x. \quad (77)$$

(In axisymmetry, the minimum was taken also over the angular coordinate y). As is clear from the formula, this restricts the change of R with Δu in the ingoing null direction, compared to the change with Δx in the outgoing null direction. $\Delta u = \Delta u_1$ with $C_1 = 0.1$ was used in all simulations in Paper II (although this was not stated there). These simulations used the eR formulation, and were stopped as soon as $\max_x C \geq 0.99$. As $C = 1$ implies $R_{,x} = 0$, $\Delta u_1 \rightarrow 0$ as $\max_x C \rightarrow 1_-$.

The hierarchy equations are in effect ODEs in x , while the time update takes the form (74). Hence

a necessary condition for the stability of our explicit scheme is that these advection equations obey the Courant-Friedrichs-Levy (CFL) condition. We guarantee this by restricting the timestep to

$$\Delta u_2 := C_2 \left(\max_x |B| \right)^{-1} \Delta x \quad (78)$$

for some $C_2 \lesssim 1$. In all our gauges $R_{,u} = 0$ at $R = 0$, and so (77) and (78) with $C_1 = C_2$ are equivalent at the centre.

Since Paper II, we have realised that using $\Delta u = \Delta u_1$ may be an unnecessarily small timestep. We have found that $\Delta u = \Delta u_2$ with $C_2 = 0.1$ also leads to stable evolutions up to close to the apparent horizon, but with fewer timesteps overall.

As the apparent horizon is approached, $\Delta u_1 \rightarrow 0$, and so this timestep does not allow us to evolve through the horizon. The alternative timestep Δu_2 remains finite, and the evolution remains stable, but as the solution changes very rapidly with u at the horizon, Δu_2 gives large errors there. (In Appendix D we remind the reader that R on constant- u time slices deviates from the horizon radius exponentially in x , and this in turn means that ΞR near the horizon grows exponentially in x .)

This problem was already noted by Burko and Ori in [7] in simulations in spherical symmetry in double null coordinates. They were able to address it in an elegant way: their code advances an ingoing null slice in v , so that, for computational purposes, v is the “time” coordinate, not u . The necessary mesh refinement in u near the horizon is then made adaptively, by splitting grid cells in u near $u = u_h$, increasingly finely as v increases.

In our framework, we could in principle introduce adaptive mesh refinement to better resolve the event horizon, but this goes against our main motivation for using null coordinates in the first place, which is to resolve type-II critical collapse down to arbitrarily small scales by adapting the coordinates to self-similarity, without the need for explicit adaptive mesh refinement.

Hence to maintain accuracy through $u = h_h$, we just reduce the global timestep near the horizon. This works because near the horizon the solution changes rapidly in u but not in x . In type-II critical collapse, most of the computation is in the approximately self-similar phase, and so is not affected by this relatively inefficient method of mesh refinement. After some experimentation we have come up with the timestep

$$\Delta u_4 = \min(\Delta u_2, \Delta u_3), \quad (79)$$

where

$$\Delta u_3 := C_3 \frac{\max_x R}{\max_x |R_{,u}|}, \quad (80)$$

with $C_3 = 0.001$. Note Δu_3 and hence Δu_4 is not proportional to Δx , in contrast to Δu_1 and Δu_2 .

If we want to evolve through a horizon, where $R_{,x} = 0$, we cannot use the numerical time step Δu_1 . In double-null gauge $B = 0$, the time step Δu_2 is not defined. The time steps Δu_3 and Δu_4 cannot be used

for convergence testing as Δu_3 is independent of Δx . As an alternative to all these, for example if we want to test convergence of a solution in double-null gauge where $R_{,x} = 0$ occurs, we also use the simple fixed timestep

$$\Delta u_0 := C_0 \Delta x. \quad (81)$$

D. Singularity excision

In the integration of the hierarchy equations from $x = 0$, information propagates only from smaller to larger x . The same is true for the time evolution equations (74), wherever $B < 0$. Our discretisation of the hierarchy and evolution equations respects this causality. In spherical symmetry, we can therefore use a crude type of singularity excision where we excise gridpoints $i \geq i_{\text{exc}}$, where i_{exc} is the first grid point where either $R_i < 0$ or $R_i < R_{i-1}/2$. (The second criterion makes sure that the first non-excised point is not too close to $R = 0$.) It is essential that we re-determine i_{exc} after each time we have solved (40) for R , that is, in all sub-timesteps. Obviously i_{exc} is not allowed to decrease from one sub-timestep to the next, or from one full timestep to the next.

Once excision starts, the excision radius $x_{\text{exc}}(u) := i_{\text{exc}}(u) \Delta x$ decreases quickly to zero. Once it is smaller than x_0 , our upwind differencing is still to the right at the outer boundary. To avoid this, we adjust x_0 so that it remains the same fraction of the excision radius x_{exc} as it was originally to x_{max} .

V. TESTS WITH A REGULAR CENTRE

A. Charged initial data

We set initial data of the form

$$\psi(0, x) + i\chi(0, x) = p\mathcal{A} e^{-(\frac{x-x_c}{d})^2 + i\omega(x-x_c)}, \quad (82)$$

so that for $\omega = 0$ the scalar field is purely real, and hence for small ω we expect the charge to be proportional to ω . With a charged scalar field, q sets an inverse length scale in the field equations, so qx_c , qd and q/ω are all relevant dimensionless parameters. This also means that changing $q \rightarrow \lambda q$ is equivalent to $x_c \rightarrow x_c/\lambda$, $d \rightarrow d/\lambda$, and $\omega \rightarrow \lambda\omega$, and similarly for any other length scales in the initial data. Therefore, it may be convenient to fix a length scale in the initial data, such as one of x_c , d and ω in (82), and consider q as a parameter of the initial data in its place (rather than a constant of nature). Thus, in one test below, we keep x_c , d and ω the same and vary q . Varying q has the conceptual advantage that for given initial data $\psi(x)$, $\chi(x)$ and $R(x)$ or $G(x)$, $Q(x)$ in the initial data is manifestly proportional to q .

B. Convergence tests

For convergence testing, we have focused on the initial data (82) with $x_c = 0.5$, $d = 0.5$, $\omega = 2.0$, and the

coupling constant $q = 1/\sqrt{4\pi}$. We complete the initial data either with $G = 1$, and then set $p\mathcal{A} = 0.15$, or with $R = x$, and then set $p\mathcal{A} = 0.2$. These amplitudes are chosen so that $\max_x C \simeq 0.5$ in the initial data at $x \simeq 1.2$.

Our numerical domain is determined by the choices $x_{\max} = 4.0$ and $x_0 = 3$. Both initial data sets collapse promptly. In the evolution $\max_x C \simeq 0.9$ is reached at $u \simeq 0.6$ at $x \simeq 1.2$, and the event horizon is crossed soon after. In these two solutions, the time step does not need to be reduced very much to resolve the horizon (in contrast to near-critical collapse). For each set of initial data, we evolve with the eR, eG and fe formulations. We thus have six combinations of initial data and formulation to consider.

We evolve with $N_x = 100 \cdot 2^n$ grid points for $n = 0\dots 8$. We choose the timestep Δu_4 with parameters $C_2 = 0.1$, $C_3 = 10^{-3}$. We output all variables at intervals $\Delta u = 0.1$, adjusting the last timestep before each output time down in order to hit it exactly. We evolve up to horizon formation, and compare resolutions up to the last output time before that. Our convergence testing methods are summarised in Appendix G. Near the horizon, the timestep Δu_4 can be smaller than the timestep Δu_2 that is by definition proportional to Δx . This does not seem to affect second-order convergence, presumably because the finite-differencing error in x dominates over that in u .

We have used convergence testing to experiment with fitting expansions near $x = 0$ of the evolved functions ψ , χ , R/x and/or G to different numbers of points, and to linear or quadratic functions, and independently with expanding the solutions of the hierarchy equations near $x = 0$ to first or second order, and for different numbers of points before our midpoint integration rule is applied. For this experimentation, we have found it helpful to first focus on the initial data, solving only the hierarchy equations, and to make decisions for one hierarchy equation at a time, in the order in which they are solved.

We eventually decided to expand some variables to second order, in the sense that we expand as far as we can using quadratic fits of ψ , χ , R/x and/or G . We then use the results of those quadratic fits, even where we expand only to first order. With that settled, we experimented with the order of expansion and the number of points to expand to, for each variable, in the order in which they are computed. We found that for all variables, expanding only to $i = 1$, and finding $i = 2, 3\dots$ by integration, was optimal. For most variables, expanding only to first order was optimal. These are the variables for which the errors $h^2 f_2$ and $h^3 f_3$ defined in (G2) below are finite at $x = 0$.

When expanding $R\hat{\Xi}\psi$ and $R\hat{\Xi}\chi$ to first order, we found that the errors f_2 and f_3 of $\hat{\Xi}\psi$ and $\hat{\Xi}\chi$ diverge as x^{-1} . This is not in itself a problem, as $h^2 f_2(x_i) \simeq h^2/(ih) = h/i$, so even at $i = 1$ the error goes down as h . However, we find that by expanding $R\hat{\Xi}\psi$ and $R\hat{\Xi}\chi$ to second order, we can essentially remove the $h^2 f_2$ error, so that the error is dominated by $h^3 f_3$. This reduces the actual error at $i = 1$ by two or three orders of magnitude already at $h = 0.04$, and by more

at higher resolution.

We have also output the quantities Q/R^3 , M/R^3 and \tilde{M}/R^3 and tested their convergence. Again, they converge to second order, but the errors go as x^{-1} , x^{-2} and x^{-1} , respectively, at the centre. This is why we use \tilde{M}/R^3 where we need to evaluate M/R^3 . The correction factors in integration Q and \tilde{M} in Eq. (76) are essential for reducing the error in Q/R^3 and \tilde{M}/R^3 from x^{-2} to x^{-1} .

Comparing M computed from (31) and (32) with $\tilde{M} = \int M_{,x} dx$, where $M_{,x}$ is given by (34), or \mathcal{M} with $\tilde{\mathcal{M}}$, tests the consistency of several of our field equations, as well as their discretizations.

With the methods discussed above, we achieve, roughly speaking, second-order pointwise convergence almost until the horizon is crossed. (We lose convergence at the horizon simply because some variables change very rapidly across the horizon, while the u -value of the horizon depends on the resolution.)

To state our convergence results more precisely, it is useful to split all variables into two groups. The variables in the first group, including R , Q , A , M , \tilde{M} , and V (in eR and eG) show clear pointwise second-order convergence including at the centre.

The variables in the second group, including ψ , χ , $\ln G$, $\ln(-2\Xi R)$, $\Xi\psi$, $\Xi\chi$, C , $x^2 M/R^3$, $x\tilde{M}/R^3$, \mathcal{H} , $\Xi \ln G$, xQ/R^3 , $M - \tilde{M}$, and V (in fe), show clear pointwise second-order convergence, except near the centre. For these variables, the dominant error looks like $h^2 \hat{f}_2(u, i)$ for the first few grid points (where i is the grid index), transitioning to the expected $h^2 f(u, x)$ at larger i . This still implies convergence in any function norm.

We note in passing that at $u = 0$, where ψ , χ and either R or G or both are still exact, $\Xi\psi$ and $\Xi\chi$ converge to third order.

The results for the six combinations of initial Bondi gauge or initial affine gauge with the eR, eG and fe formulations are broadly similar.

In order to test the Raychaudhuri equation $E_{xx} = 0$, we have also discretized

$$E_{xx(1)} := GV_{,x}, \quad (83)$$

$$E_{xx(2)} := -4\pi R(\psi_{,x}^2 + \chi_{,x}^2), \quad (84)$$

using a different method from elsewhere in the code. This means in the eR or eG formulations, where G or R , respectively, are found by solving $E_{xx} = 0$, we have a non-trivial test of the discretization of that process. In the fe formulation, we have a test of the discretization of the solution of $E_{xx} = 0$ for either R or G in the initial data, combined with a test of how the subsequent free evolution error leads to increasing violation of the constraint $E_{xx} = 0$. We find that $E_{xx(1)} - E_{xx(2)} = 0$ converges to second order, except at the boundaries, where it is only first-order. This is because there we use second-order accurate but one-sided finite differences in evaluating the constraint, and therefore in self-convergence testing at the boundaries we compare a one-sided derivatives at the lower resolution with a centred derivative at the higher resolution.

For all variables, we have also taken the three differences of the numerical solutions in the three formulations, and again we find second-order convergence, with errors of the order of magnitude of the self-convergence errors in each formulation. In other words, all three formulations converge to the same continuum solution, as expected.

C. Evolving through the event horizon and singularity excision

We have further evolved the initial data that we already used for convergence testing through the horizon, obviously in eG and fe only. We lose pointwise convergence there, but the solutions in eG and fe remain qualitatively alike. On each time slice beyond the event horizon, R increases from zero to a maximum that marks the apparent horizon, then decreases back to zero at some $x = x_s(u)$ which denotes the spacelike curvature singularity, with $dx_s/du < 0$. We excise grid points with $x > x_s(u)$, which are no longer physical. The code remains stable and appears accurate up to within very few grid points of the singularity.

As $x \rightarrow x_s$, $R_{,x}$ and G diverge. We therefore also plot against u and λ . We find that R then decreases essentially linearly with λ everywhere inside the apparent horizon until we lose resolution near the singularity.

Inside the apparent horizon, $\mathcal{M} \simeq 0.21$ and $Q \simeq 0.023$ appear essentially constant, compared to R . If \mathcal{M} and Q were exactly constant, the spacetime would be locally isometric to Reissner-Nordström spacetime, and with $Q \neq 0$ the singularity at $R = 0$ should then be timelike, and preceded by a Cauchy horizon. However, where we excise, R is still a significant fraction of the event horizon radius $r_+ := \mathcal{M} + \sqrt{\mathcal{M}^2 - Q^2} \simeq 2\mathcal{M}$, while the Cauchy horizon radius $r_- := \mathcal{M} - \sqrt{\mathcal{M}^2 - Q^2} \simeq Q^2/(2\mathcal{M})$ is smaller by a factor of about 10^{-4} , so we lack resolution for seeing the Cauchy horizon.

Clearly, our code is not yet very suitable for exploring aspects of charged black hole interiors such as Cauchy horizons and mass inflation, but that is not its purpose at the moment. Rather, we want to demonstrate that we can evolve into a region where outgoing null cones reconverge.

D. Type-II critical collapse of a spherical charged scalar field

As our emphasis in this paper is on developing methods for simulating type-II critical collapse on null cones beyond spherical symmetry, rather than on charged collapse in spherical symmetry in detail, we examine only four one-parameter families of initial data. In the first of these, $\phi(0, x)$ is given by (82) with $x_c = 1.5$, $d = 0.5$, $\omega = 2.0$ and $\mathcal{A} = 0.05$, and we initialise the radial gauge with $G(0, x) = 1$. We set the coupling constant to $q = 1/\sqrt{4\pi} \simeq 0.2821$.

The second family is as the first except that we initialise the radial gauge with $R(0, x) = x$. As already $R_{,x}(0, x) \simeq 1$ in the first family, these two families do not differ qualitatively. The third family is again like the first, except that we set $\omega = 0$, so that the scalar field is real and $Q = 0$. The fourth family is again like the first, except that we set $q = 10/\sqrt{4\pi} \simeq 2.821$, so that $Q(0, x)$ is 10 times as large.

During the evolution, we use sdn gauge, given in (60), with the parameter x_0 adjusted so that $x = x_0$ is approximately the past light cone of the accumulation point of echos in near-critical solutions.

Numerically, we use either the eR or eG formulation. We have not tried the fe formulation in critical collapse, as we expect the slow drift away from the regularity condition $R_{,x} = G$ at the centre to affect the correctness of near-critical evolutions. As for numerical parameters, we use a uniform grid in x with $x_{\max} = 5$ and $N_x = 250$ grid points, and the timestep (79) with $C_2 = 0.1$ and $C_3 = 0.001$.

For the $G = 1$ initial data, we chose $x_0 = 3.17$ in both the eR and eG formulation. We found $p_* \simeq 0.91$. The initial mass and charge at $p \simeq p_*$ are $\mathcal{M} = 0.151$ and $Q \simeq 0.021$.

For the $R = x$ initial data, we chose $x_0 = 3.107$ in the eR formulation and $x_0 = 3.103$ in the eG formulation. We found $p_* \simeq 1.01$. The initial mass and charge at $p \simeq p_*$ are $\mathcal{M} = 0.173$ and $Q \simeq 0.026$.

The results for the two families of initial data are qualitatively similar, as one would expect. The results for the eR and eG formulations, for the same initial data, are quantitatively very similar, as one would expect from the convergence tests. In the following, for conciseness we present results only for the $G = 1$ family of initial data, evolved with the eG formulation.

As a proxy for the black hole Hawking mass and charge, which are strictly speaking defined at future null infinity, we evaluate \mathcal{M} and Q on the first symmetry 2-sphere where the Hawking compactness takes the value $C(u, x) = C_{\text{thr}}$. (“First” here means the smallest such u .) In the results presented here in the eG formulation, we choose the obvious value $C_{\text{thr}} = 1$, but this is not possible in the eR formulation. We discuss the role of the choice of C_{thr} in Sec. V F.

The fine-structure of critical scaling on the dispersal side of the threshold of collapse is shown in Fig. 1 for the curvature invariant T . On the collapse side, Figs. 2 and 3 show the fine-structure for \mathcal{M} and Q of the first (approximate) marginally outer-trapped surface (from now on, MOTS and FMOTS for the first MOTS). What we actually plot is $-1/2 \ln T - \gamma \ln(1 - p/p_*) + A$ in Fig. 1, $\ln \mathcal{M} - \gamma \ln(1 - p/p_*) + A$ in Fig. 2, and $\ln Q - \mu \ln(1 - p/p_*) + A$ in Fig. 3. The family-dependent offset A has been fitted so the average of $-1/2 \ln T - \gamma \ln(1 - p/p_*) + A$ is roughly zero at high fine-tuning. γ and μ have been set to their theoretically predicted approximate values $\gamma = 0.374$ and $\mu = 0.883$ [27].

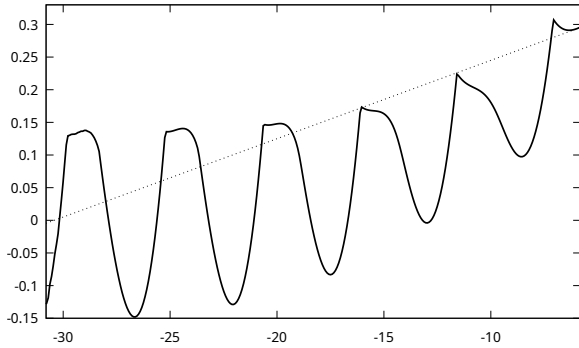


FIG. 1. Maximum curvature fine-structure for the $G = 1$ family of initial data, in the eG formulation: we plot $-1/2 \ln |\max T| - \gamma \ln(1 - p/p_*) + A$ against $\ln(1 - p/p_*)$. We use the approximate theoretical value $\gamma = 0.374$, and the family-dependent offset $A = -0.23$ has been fitted by eye so that the average of the fine-structure is approximately zero at high fine-tuning to the threshold of collapse, (that is, in the limit $|p - p_*| \rightarrow 0$). The range of $\ln(1 - p/p_*)$ on the horizontal axes has been chosen as in Fig. 1 of Paper II for comparison. (As in Paper II, we have suppressed axis labels to make figures larger.) The thin dotted line has been fitted by eye to the first two peaks from the right and has slope $\delta\gamma = 0.012$, meaning that the curvature critical exponent is slightly larger at low fine-tuning

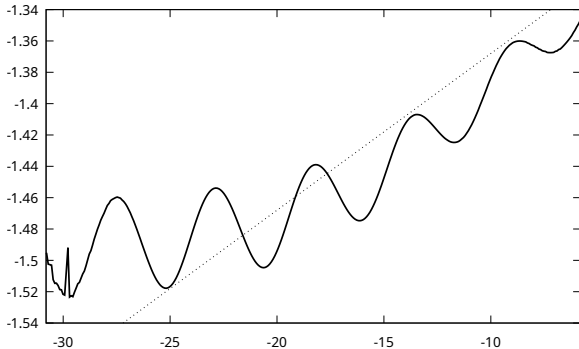


FIG. 2. Black hole mass fine-structure for the $G = 1$ family of initial data, in the eG formulation, with $C_{\text{thr}} = 1$: we plot $\ln M - \gamma \ln(p/p_* - 1) + A$ against $\ln(p/p_* - 1)$. γ and A and the horizontal range are as for the curvature scaling plot in Fig. 1. Compare also Fig. 2 of Paper II. The thin dotted line has been fitted by eye to the first two peaks from the right. It has slope $\delta\gamma = 0.010$, meaning that the mass critical exponent is slightly larger at low fine-tuning, in line with that for the curvature, to within a plausible fitting error.

E. The effect of charge on the critical scaling

At high fine-tuning, the fine-structures are periodic, thus confirming the values of γ and μ from perturbation theory. The fine structure for T has the same amplitude of about 0.15 and shape as in Fig. 1 of Paper II, which showed T for a one-parameter family of real, spherically symmetric initial data. At low fine-tuning, the curve has the same periodic structure but rises slightly with $\ln(1 - p/p_*)$. The same observation

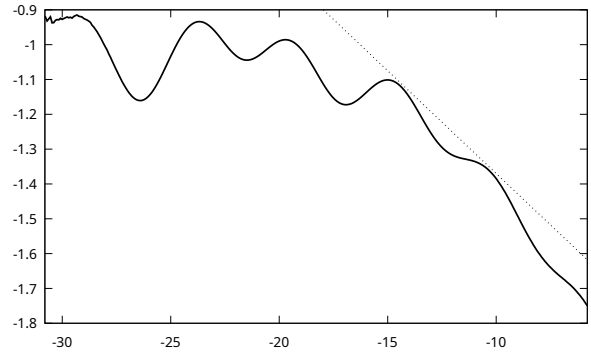


FIG. 3. Black hole charge fine-structure for the $G = 1$ family of initial data, in the eG formulation, with $C_{\text{thr}} = 1$: we plot $\ln Q - \mu \ln(p/p_* - 1) + A$ against $\ln(p/p_* - 1)$. We have used the approximate expected critical exponent $\mu = 0.883$, and A as in the curvature scaling plot in Fig. 1. The thin dotted line has been fitted by eye to the first two peaks from right. It has slope $\delta\mu = -0.059$, meaning that the charge critical exponent is smaller at low fine-tuning. It is plausible from this figure that at high fine-tuning the expected value of μ is achieved. The fine-structure has approximately the same period as for the curvature and mass, as one expects.

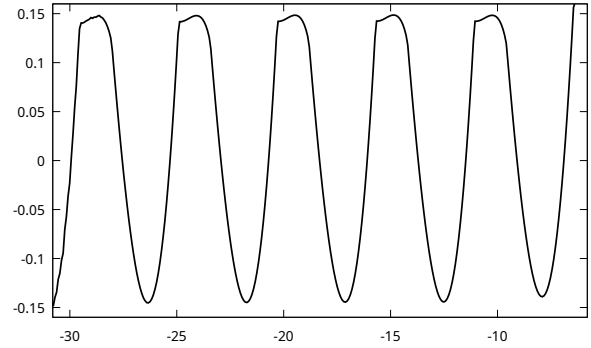


FIG. 4. Maximum curvature fine-structure for the $G = 1$ family of *real* initial data, in the eG formulation. We set $A = -0.58$, otherwise as in Fig. 1.

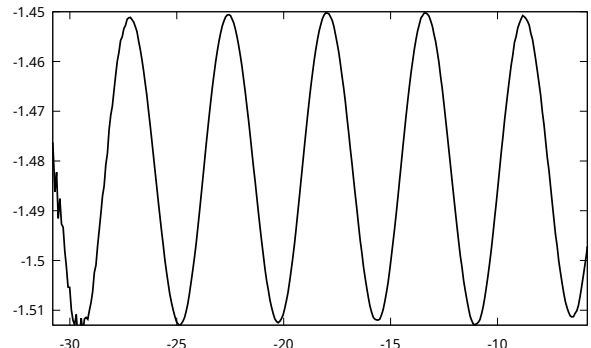


FIG. 5. Black hole mass fine-structure for the $G = 1$ family of real initial data, in the eG formulation, with $C_{\text{thr}} = 1$. We set $A = -0.58$, otherwise as in Fig. 2.

applies to the periodic fine structure of M . It has an amplitude $\simeq 0.03$. From Fig. 3, the fine structure in $\ln Q$ evaluated also appears to be continuous, with amplitude $\simeq 0.15$.

The value of μ predicted in [27] was verified in collapse simulations in [13] and [28], and is verified here again by us to be correct sufficiently close to the threshold of collapse. Figures in these last two papers showed a power law with a wiggle, but did not show the wiggle clearly. Hence our Fig. 3 is the first plot of the fine structure of the charge scaling law for any physical system, here the spherical charged scalar field.

At low fine-tuning, we see deviations from the expected scaling laws. Heuristically, these can be described as modifications of the critical exponents γ and μ (as we did for the critical exponents for the mass and angular momentum in [29]). To quantify these modifications, we have fitted the thin dotted lines in Figs. 1, 2 and Fig. 3 by eye. These have slopes of $\delta\gamma = 0.012$, $\delta\gamma = 0.010$, and $\delta\mu = -0.059$, respectively. Note the values of $\delta\gamma$ on the dispersion and collapse sides are roughly the same, as one would expect, but the fitting by eye is somewhat arbitrary. As in [29], the small change in critical exponent is a convenient quantitative way of describing the fine structure at low fine-tuning, but we do not have a quantitative explanation for it.

For comparison, we have also fine-tuned a family of real, and therefore uncharged, initial data with $G = 1$, differing from our charged data only by the choice $\omega = 0$. We also set $\mathcal{A} = 0.075$ in order to make $p_* \simeq 1$. For the eG formulation, we chose $x_0 = 3.525$ and found $p_* \simeq 0.95$. For the eR formulation, we chose $x_0 = 3.530$ and found $p_* \simeq 0.94$. The fine-structure for T and M (in the eG formulation, with $C_{\text{thr}} = 1$) is given in Figs. 4 and 5. Here we can read off more accurately that the amplitude of the fine structure for M is $\simeq 0.032$. As already noted in Paper II, this differs significantly from the values for the amplitude given in the literature. It is remarkable how periodic both fine-structures are already at low fine-tuning, in contrast to the charged case, where $|Q|/M$ has to be quite small before the critical exponents agree with their values calculated in perturbation theory in [27]. That calculation considered charge as a linear perturbation on an uncharged background critical solution (the Choptuik solution). From Figs. 1, 2 and 3, this seems to be accurate for $\ln|1 - p/p_*| \lesssim -20$. This corresponds to $|Q|/M \lesssim 10^{-4}$ for the black hole.

So far we have presented results only for a single one-parameter family of charged initial data, which tells us nothing about universality. Both the mass and charge critical exponents appear to agree with their predicted values, however, which is indirect evidence of their universality. We also find that the fine-structure of the mass scaling law looks very similar in the charged and uncharged families. By considering a more highly charged family, we have found initial evidence that the fine-structure of the charge scaling law may not be universal.

We consider again complex Gaussian initial data with $x_c = 1.5$, $d = 0.5$, $\omega = 2.0$ and $\mathcal{A} = 0.05$,

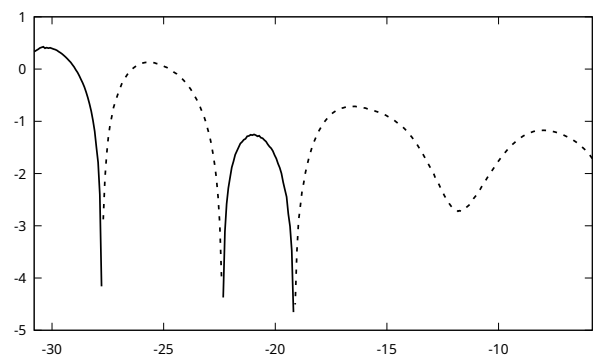


FIG. 6. Charge fine-structure for a different family of complex Gaussian initial data (in the eG formulation, with $C_{\text{thr}} = 1$.) The initial scalar field profile is the same, and again $G = 1$ in the initial data, but q is larger by a factor of 10, compared with the family represented in Fig. 3. For plotting, we set $A = -0.23$, otherwise as in Fig. 3. The charge is positive where the curve is solid and negative where the curve is dashed. (The kinks in $\ln|Q|$ are where Q goes through zero.) This is qualitatively different from Fig. 3, where the charge is always positive.

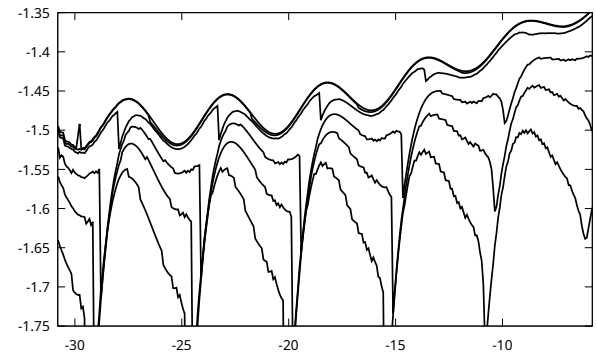


FIG. 7. The fine structure of M , for the $G = 1$ family of initial data, in the eG formulation, but now for different values of C_{thr} . From bottom to top, the curves correspond to $C_{\text{thr}} = 0.8, 0.9, 0.95, 0.99, 0.999$ and 1, as in Fig. 8. The $C_{\text{thr}} = 0.999$ and 1 curves are almost indistinguishable, but there is a tiny jump once per period in the $C_{\text{thr}} = 0.999$ curve. The $C_{\text{thr}} = 1$ curve is the same as in Fig. 2.

with initial gauge $G(0, x) = 1$. The only difference is that we now set $q = 10/\sqrt{4\pi} \simeq 2.821$, 10 times the value we investigated before. (As q has dimension of inverse length, this is equivalent to keeping q fixed and changing all other length scales in the numerical domain and initial data by factors of 10.) We find $p_* \simeq 1.157$. Once again we find charge scaling roughly with $\mu = 0.883$, but the sign of the charge now oscillates in $\ln(p - p_*)$. The charge fine-structure is shown in Fig. 6. The mass scaling, by contrast, is unchanged (and therefore we do not show it here). We will return to this non-universality elsewhere.

F. The role of the collapse criterion

In the eG and fe formulations we can choose $C_{\text{thr}} = 1$, but not in the eR formulation. In Paper II, for

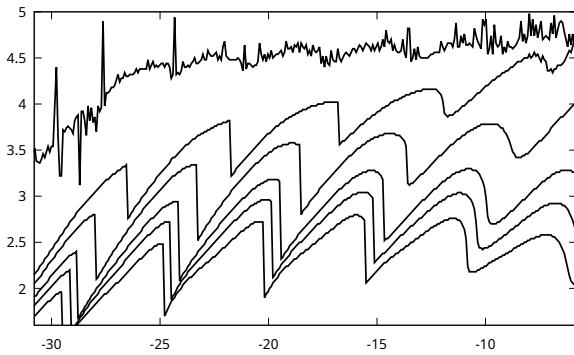


FIG. 8. Location $x = x_C$ of the symmetry sphere (u_C, x_C) where we evaluate M and Q , for the $G = 1$ family of initial data, in the eG formulation, but now for different values of C_{thr} . From bottom to top, the curves correspond to $C_{\text{thr}} = 0.8, 0.9, 0.95, 0.99, 0.999$ and 1 .

example, where we used the eR formulation, we used $C_{\text{thr}} = 0.99$ in spherical symmetry and for mildly non-spherical initial data, and $C_{\text{thr}} = 0.8$ for the most-nonspherical initial data, and found that the mass fine-structure was discontinuous, including in spherical symmetry.

To demonstrate the effect of the value of C_{thr} on the measured M and Q , Fig. 7 shows the mass fine-structure obtain with different values of C_{thr} . From bottom to top, the six curves correspond to $C_{\text{thr}} = 0.8, 0.9, 0.95, 0.99, 0.999$ and 1 of C . The curves for $C_{\text{thr}} < 1$ are discontinuous once per period, but the curve for $C_{\text{thr}} = 1$ is continuous. (The jump in the curve for $C_{\text{thr}} = 0.999$ is just about visible.) Similar jumps are seen in the fine-structure of Q .

Fig. 8 shows the x -location of the first symmetry 2-sphere (u_C, x_C) where $C(u_C, x_C) = C_{\text{thr}}$, for the same values of C_{thr} . For each C_{thr} , this location is discontinuous at the same values of $\ln(p/p_* - 1)$ where $\ln M$ and $\ln Q$ also jump. The jump in x_C is still large for $C_{\text{thr}} = 0.999$. This suggests that, with $C_{\text{thr}} < 1$, the jumps in M and Q at periodic values of $\ln(p/p_* - 1)$ are caused by the jumps in x_C at the same values.

The exception is the location x_C of the first occurrence of $C = 1$: it is a very noisy function of $\ln(p/p_* - 1)$, but with no obvious jumps. The noisiness is explained by the difficulty of locating the first occurrence of $C = 1$: in practice, we find the x -location where C goes through 0 at the first timestep where its maximum is larger than 1. Note that M and Q read off at this noisy location are not visibly noisy in Figs. 2 and 3: we believe this is explained by the fact that M and Q , as functions of x along the curve $C = 1$ (the apparent horizon) quickly asymptote to M_{BH} and Q_{BH} , and so the values of M and Q read off at $x = x_C$ depend only weakly on x_C .

We can understand theoretically why the mass fine-structure *in spherical symmetry* is continuous for $C_{\text{thr}} = 1$ but discontinuous for $C_{\text{thr}} < 1$. We expect the function $C(u, x; p)$ to be continuous in all its arguments. Nevertheless, the set of points (u, x) where $C(u, x; p) = C_{\text{thr}}$ is in general discontinuous in p , a simple example of catastrophe theory. The same is therefore true for the point in this set with the small-

est value of u .

However, $C_{\text{thr}} = 1$ in spherical symmetry is an exception to this generic behaviour, because $C(u, x; p) = 1$ is the apparent horizon, which divides spacetime into a trapped and an untrapped region, so it cannot jump in p .

Beyond spherical symmetry, a 2-sphere with $C = 1$ is not in general marginally trapped, and so does not lie in the apparent horizon. Therefore we generically expect the mass of the first coordinate 2-sphere with $C = 1$ to jump in p . We will test this when we apply the eG formulation to axisymmetric critical collapse elsewhere.

As a practical discovery, we find that plotting the equivalent of Fig. 8 just for the data points obtained in a bisection to p_* allows us to quickly find the appropriate value of x_0 : if these curves drop to $x = 0$ with increased fine-tuning, our choice of x_0 is too large. If they rise to $x = x_{\text{max}}$ then x_0 is too small. To find p_* and x_0 , we then alternate an automated bisection in p (to machine precision) with an adjustment of x_0 by hand (to about two to four digits).

VI. TESTS ON A NULL RECTANGLE

A. Previous work

We now test evolutions with null data given on an intersecting outgoing null cone $u = u_0$, for $v_0 \leq v \leq v_1$ (the “right boundary”), and an ingoing null cone $v = v_0$, for $u_0 \leq u \leq u_1$ (the “left boundary”). These data determine the solution on the “null rectangle” $u_0 \leq u \leq u_1, v_0 \leq v \leq v_1$.

Simulations on null rectangles have been used in [6, 8, 15] to study black hole interiors in the simpler case of the spherical Einstein-Maxwell-*real* scalar field system.

By contrast, in [31], the spherical Maxwell-charged scalar system is evolved on a *fixed* RN spacetime, in order to investigate event horizon instabilities. That work uses double-null coordinates, compactified to both past and future null infinity (but finite across the past and future event horizon) as in [8]. It uses the electromagnetic gauge $\nabla_a(R^{-2}A^a) = 0$, or $A_{u,v} + A_{v,u} = 0$ in double-null coordinates, in contrast to our electromagnetic gauge $A_x = 0$, which in double-null coordinates becomes $A_v = 0$.

We are aware of only one previous numerical treatment of the full Einstein-*charged* scalar system in spherical symmetry: in [30], the evolution is on hyperboloidal *spacelike* slices that on the left end are truncated with an excision boundary inside the event horizon of a RN black hole, and at their right end extend to future null infinity.

We believe the present paper gives the first algorithm for simulating the spherical Einstein-Maxwell-charged scalar system in null coordinates, allowing for simulations both on a null rectangle or with a regular centre.

B. Physical setup

We evolve by advancing in u , considered as our time coordinate, as before, with the left boundary identified with $x = 0$. We refer to quantities such as $R_* := R(u_0, v_0)$ as the ‘‘corner data’’ and denote them by an asterisk. The details of how consistent left and right data are found are given in Appendix E, and the discretisation of that algorithm in Appendix F. Here we only summarise our free data and gauge choices. On the left boundary, we choose $B = 0$ (so that the left boundary is null), $G = G_*$ (so that u is an affine parameter on the left boundary), and $A = 0$ (an electromagnetic gauge choice). On the right boundary $u = 0$, we choose the $G = G_*$ (so that x is an affine parameter there). We can freely specify ψ and χ on the left and right boundaries, the gauge-independent corner values R_* , \mathcal{M}_* and Q_* , and any two out of the three gauge-dependent corner values G_* , $R_{,x*}$ and $R_{,u*}$.

Our algorithm also allows us to fix the right spacetime gauge as $R_{,x} = R_{,x*}$, but for brevity we do not present results here. When there is no scalar field on the right boundary, Bondi and affine gauge are equivalent there anyway. Moreover, in our discretisation they are equivalent without discretisation error.

We can continue the spacetime gauge into the numerical domain with any choice of $B(u, x)$ (as long as $B = 0$ on the left boundary), but again for brevity we only present double-null gauge $B(u, x) = 0$, so that x is an ingoing null coordinate everywhere, and the numerical domain is the full domain of dependence of the data (a null rectangle). We use the timestep $\Delta u_0 = C_0 \Delta x$, with $C_0 = 0.1$.

We shall restrict to scenarios where $C_* < 1$, so that the corner 2-sphere is untrapped. Then $R_{,x*} > 0$ gives us $R_{,u*} < 0$, and the ingoing Raychaudhuri equation (49) gives us $R_{,u} < 0$ on the entire left boundary. We also restrict to the case where the entire right boundary is untrapped, so that $R_{,x} > 0$ there.

C. Prompt collapse

Consider a null rectangle with $R_* > 0$, $R > 0$ on the left boundary, $M_* = Q_* = 0$, zero scalar field on the left boundary, and no trapped surface on the right boundary. Then the triangular region bounded by the regular centre $R = 0$, $u = u_0$ and $v = v_0$ is a piece of Minkowski spacetime, and $u = u_0$ can be extended to the left to $R = 0$, with vanishing scalar field.

If the data on $u = 0$ are sufficiently strong that a MOTS first forms at (v_1, u_{FMOTS}) for some $u_0 < u_{\text{FMOTS}} < u_1$, then there must be an event horizon at some $u = u_{\text{EH}}$ with $u_0 < u_{\text{EH}} \leq u_{\text{FMOTS}}$. We have in effect simulated gravitational collapse from initial data on a null cone with regular centre, while actually solving the Einstein equations only on a null rectangle, and thus avoiding the complications of a regular centre. The null rectangle may then be truncated by a curvature singularity ‘‘at the top’’. Figs. 9 and 10 show gravitational collapse from data on a single null cone, and from data on two intersecting null cones.

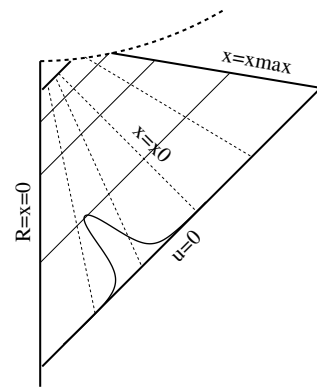


FIG. 9. Spacetime diagram illustrating collapse from initial data on an outgoing null cone, with singularity excision. The regular centre and numerical domain are shown as bold lines, the singularity as bold dashed, lines of constant u as thin solid, and lines of constant x as thin dashed. The lines of constant x illustrate sdn gauge, with $x = 0$ the timelike regular centre $R = 0$, $x = x_0$ ingoing null, and $x = x_{\max}$ future spacelike. Initial data can be imposed on the outgoing null cone (with regular centre) $u = 0$, symbolised here by a bell curve.

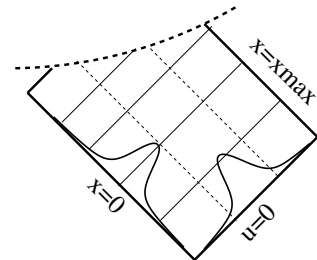


FIG. 10. Spacetime diagram illustrating the null rectangle setup, with initial data imposed on the ingoing null cone $x = 0$ and/or the outgoing null cone $u = 0$. The lines of constant u (thin solid) are outgoing null again, as in Fig. 9, but the lines of constant x (thin dashed) are all ingoing null, illustrating double-null gauge.

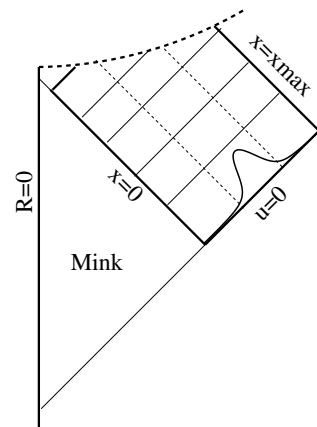


FIG. 11. Spacetime diagram illustrating what we have called ‘‘prompt collapse’’. Free initial data are imposed on $u = 0$, but the data on $x = 0$ are now specifically for Minkowski spacetime, so that the solution on the numerical domain can be continued into the triangle bounded by $R = 0$, $x = 0$ and $u = 0$ (extended as thin solid lines) as a part of Minkowski spacetime.

Fig. 11 illustrates the prompt collapse scenario. In each case, we illustrate excision of a future spacelike singularity from the numerical domain.

If, on the other hand, there is no trapped surface in the null rectangle, formation of a black hole from the regular data on $u = u_0$ is neither proved nor disproved. In particular, we do not expect to find the black hole threshold in a one-parameter family of initial data on $u = u_0$ in this setup: u_{FMOTS} will become larger than u_1 well above the collapse threshold. Another way of seeing this is to note that the critical solution in type-II critical collapse is non-vacuum both inside and outside the past null cone of its singularity.

As an example of prompt collapse, we set $\mathcal{M}_* = Q_* = 0$, $R_* = 2$, and fix the corner gauge as $G_* = R_{,x*} = 1$. With no scalar field on the left boundary, $R_{,u} = R_{,u*} = -1/2$ there, so the left boundary intersects $R = 0$ at $u = 4$. On the right boundary we set ψ to be a Gaussian with centre at $x_c = 0.5$, width $d = 0.1$, frequency $\omega = 50$ and amplitude $9.5 \cdot 10^{-3}$. We set $q = 50$ and $x_{\text{max}} = 1$. From now on, without loss of generality, we let $u_0 = 0$ and $v_0 = v$, and we identify $v = 0$ with $x = 0$. The event horizon forms just after $u = 3.3$. In the eG and fe formulations we evolve to $u = 3.9$, just before singularity excision starts, and in the eR formulation at $u = 3.3$, just before the event horizon forms.

We evolve with $N_x = 100 \cdot 2^n$ grid points, with $n = 0 \dots 4$. In all three formulations we find perfect second-order pointwise self-convergence of R and $\ln G$ already at the lowest resolution, without any of the complications caused by using expansions at a regular centre. Perfect second-order self-convergence persists through the event horizon and until excision starts, and even during excision breaks down only near the excision boundary. The pairwise differences between the three formulations similarly show perfect second-order pointwise convergence.

D. Schwarzschild and extremal Reissner-Nordström

In our gauge, the vacuum Schwarzschild solution is already a non-trivial test, but with an exact solution available, see Appendix A. With the choice $G_* = R_{,x*} = 1$, affine and Bondi right gauge coincide, with $G = R_{,x} = 1$ on the entire right boundary. We set $M_* = 0.5$, so that the horizon radius is $r_+ = 1$, and $R_* = 2$, so that $C_* = 1/2$ and $R_{,u} = R_{,u*} = -1/4$ on the entire left boundary. We set $x_{\text{max}} = 1$. In the eR formulation we stop the evolution at $u = 3.9$, just before the event horizon $R = 1$ is crossed at $u = 4$. In the eG and fe formulations, singularity excision starts at $u \simeq 4.3$, and we stop the evolution at $u = 6$, when all grid points at $x \gtrsim 0.1$ are excised. We again evolve with $N_x = 100 \cdot 2^n$, with $n = 0 \dots 4$. We see perfect self-convergence and convergence between resolutions to the end of the simulations, that is close to the horizon in eR and well into the excision regime in eG and fe. We also see perfect convergence of all formulations against the exact solution (we have coded up the exact solution only outside the horizon).

We continue to extremal RN. We set $\mathcal{M}_* = Q_* = 1$, so that the horizon radius is again $r_+ = 1$, and we again set $R_* = 2$. M is now not constant, and in particular at the corner $M_* = 3/4$, so that $C_* = 3/4$. We again fix the gauge as $G_* = R_{,x*} = 1$. This gives us $R_{,u} = R_{,u*} = -1/8$ on the left boundary, so that the event horizon is crossed at $u = 8$, and the left boundary runs into the singularity at $u = 16$. We set $x_{\text{max}} = 1$.

On the horizon $R_{,x} = 0$ but, in contrast to the subextremal case, inside the black hole $R_{,x} > 0$ again, and the singularity $R = 0$ is now timelike. This means that our time slices of constant u run into the singularity at their left edge first. Singularity excision would not make sense, as boundary conditions would have to be imposed at the timelike singularity.

We evolve with $N_x = 100 \cdot 2^n$, with $n = 0 \dots 6$, up to $u = 7.9$ in the eR formulation, and up to $u = 14$ in the eG and fe formulations. We see perfect self-convergence and convergence between formulations in the highest resolutions, but convergence in the lower resolutions begins to break down between $u = 13$ and $u = 14$, due to the appearance of sharp gradients in all variables near the left boundary.

E. Perturbed extremal Reissner-Nordström

To simulate extremal RN perturbed by charged matter entering through the *right* boundary, we set again $\mathcal{M}_* = Q_* = 1$, $R_* = 2$, $G_* = R_{,x*} = 1$, $x_{\text{max}} = 1$, and we evolve to $u = 14$, this time only in the eG and fe formulations as we want to cross the horizon.

We set $\phi = 0$ on the left boundary, but on the right boundary we set ϕ to a complex Gaussian of the form (82) with centre at $x_c = 0.4$, width $d = 0.1$, complex phase frequency $\omega = 30$ and amplitude $5 \cdot 10^{-4}$. We set $q = 100$. Then at $u = 0$ the augmented mass rises from $\mathcal{M}_* = 1$ at $x = 0$ to $\mathcal{M} \simeq 1.0032$ at $x_{\text{max}} = 1$ (the outer boundary), and the charge from $Q_* = 1$ to $Q \simeq 1.0068$. One can interpret this as trying to overcharge a pre-existing static eRN black hole with a burst of scalar field radiation coming in from past null infinity at finite advanced time.

Not unexpectedly, this particular attempt fails. Indeed for all $u > 1.7$, already well before the putative horizon is crossed, $Q \leq \mathcal{M} \leq 1$ everywhere on the domain $0 \leq x \leq 1$ (with equality only at the left boundary). The event horizon is crossed at $u \simeq 7.4$, that is, earlier than in the unperturbed eRN solution and has radius $R \simeq 1.08$ (and hence Hawking mass $M \simeq 0.54$), augmented mass $\mathcal{M} \simeq 0.997$ and charge $Q \simeq 0.993$, so the final black hole is slightly subcritical.

R on our numerical domain $0 \leq x \leq 1$ levels off in x at $u \simeq 7.4$, indicating the event horizon, then has a maximum in x between $u \simeq 7.4$ and $u \simeq 8.8$, and then returns to be an increasing function of x at least up to $u = 14$, when we stop the simulation. This is illustrated in Fig. 12. That we do not see $R_{,x} < 0$ for sufficiently large x , for all $u > u_{\text{horizon}}$, is probably due to the limited size of our numerical domain. We will investigate this elsewhere.

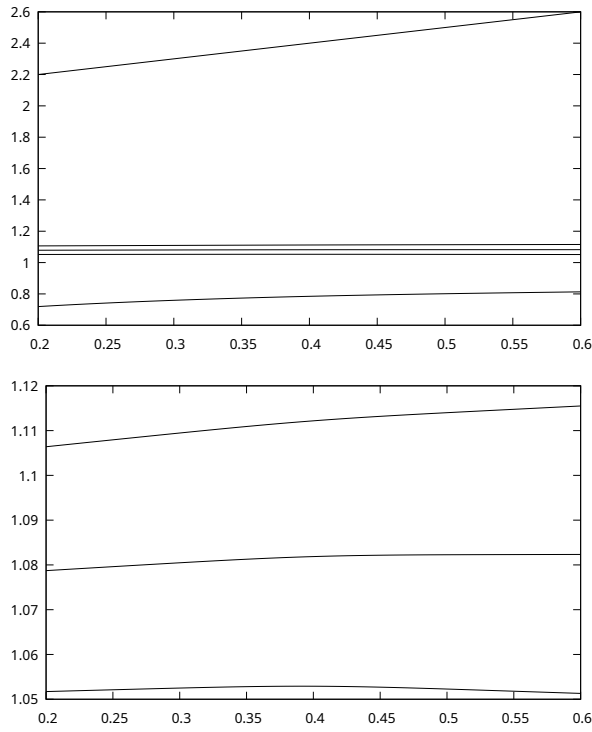


FIG. 12. Plot of the area radius $R(u, x)$ in the eRN solution perturbed by a complex Gaussian on the right boundary $u = 0$. We plot against x , at $u = 0, 7.2, 7.4, 7.6$ and 14 (from top to bottom). The lower plot shows only $u = 7.2, 7.4$ and 7.6 for clarity, demonstrating that the event horizon is crossed at $u \simeq 7.4$.

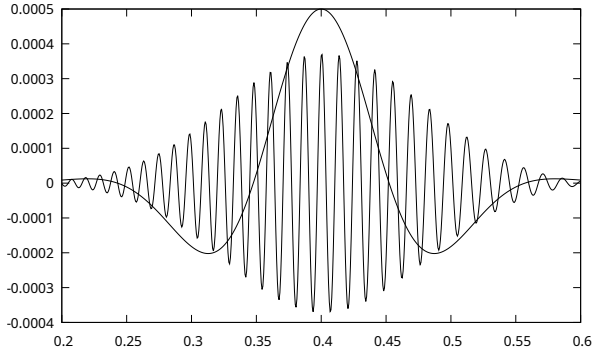


FIG. 13. Plot of the real part $\psi(u, x)$ of the complex scalar field in the eRN solution perturbed by a complex Gaussian on the right boundary $u = 0$. We plot against x , at $u = 0$ (the simpler graph) and at $u = 14$ (the highly oscillating graph). The imaginary part χ looks similar, with a phase shifting indicating that the rapid oscillation is in the complex phase. The numerical domain is $0 \leq x \leq 1$, but we plot only the range where ψ is large.

We evolve with $N_x = 100 \cdot 2^n$, with $n = 0 \dots 6$. We need the higher resolutions to see clean self-convergence and convergence between resolutions. The simulation is more demanding than that of unperturbed eRN because ϕ becomes rapidly oscillating in x . This is illustrated in Fig. 13.

To simulate extremal RN perturbed by charged matter entering through the *left* boundary, we set once again $\mathcal{M}_* = Q_* = 1$, $R_* = 2$, $G_* = R_{,x*} = 1$,

$x_{\max} = 1$, and evolve to $u = 14$ in the eG and fe formulations. We now set $\phi = 0$ on the right boundary, while on the left boundary we set ϕ to be a complex Gaussian with centre at $u_c = 4$, width $d = 0.8$, frequency $\omega = 3.75$ and amplitude $5 \cdot 10^{-4}$. (We have scaled d and ω with respect to the previous example by factors of 8 because $R_{,x*} = 1$ but $R_{,u*} = -1/8$.) We again set $q = 100$. Between $u = 3$ and $u = 5$, due to the left data, the augmented mass at $x = 0$ drops from $\mathcal{M}_* = 1$ to $\mathcal{M} \simeq 0.9982$ and the charge from $Q_* = 1$ to $Q \simeq 0.9973$, and both \mathcal{M} and Q remain almost constant in x throughout. The horizon is crossed at $u \simeq 7.7$ with $R \simeq 1.04$, that is, earlier than in the unperturbed eRN solution. Once again we know from \mathcal{M} and Q on the horizon that the black hole is actually slightly sub-extremal, but on our numerical domain R we do not see $R_{,x} < 0$ soon after the horizon is crossed.

Once again we see good convergence within formulations and between formulations at the highest resolution. At $u = 14$, the complex scalar field is rapidly oscillating in x , with about 16 phase oscillations between $x = 0$ and $x = 0.1$, with an exponentially decaying envelope, and this is only just resolved at the two highest resolutions.

VII. CONCLUSIONS

This series of papers investigates the usefulness of single null coordinates, in which surfaces of constant retarded time u are null cones and the coordinate lines of constant (u, θ, φ) are their generators. The remaining gauge freedom is how points on each generator are labelled by the radial coordinate x .

We have identified three generic formulations: the metric coefficient R is evolved and the metric coefficient G is found by solving the (outgoing) Raychaudhuri equation, or the other way around, or both R and G are evolved freely (and the Raychaudhuri equation is imposed as a constraint only at $u = 0$). In these three, any labelling of points on a null generator by the radial coordinate x is possible. Dynamically, this radial gauge choice is controlled by freely choosing B . There are also two particular formulations each tied to a specific gauge: the Bondi formulation where $R = x$, and the affine formulation where $G = 1$. These are maximally constrained, in the sense that only physical degrees of freedom are evolved.

To our knowledge, there is no clear statement in the literature that any of the three general formulations can be combined with any choice of radial gauge. This observation is the main conceptual novelty of the present paper.

The main motivation for introducing the eG and fe formulations, in which G is evolved, is that in them we can evolve through event and apparent horizons. In Paper II, both our choice of the eR formulation and our choice of lsB gauge did not allow us to do this in axisymmetric scalar collapse. This in turn meant that we could not bisect arbitrarily close to the collapse threshold in highly-nonspherical one-parameter families of initial data. In the eG and fe formulations,

we can now evolve through horizons, while still using B to make the coordinate adjust to the approximate self-similarity observed in type-II critical collapse. We plan to apply our eG formulation with a suitable radiable gauge to this problem.

To present the new formulations pedagogically, and with a focus on regularity at the central worldline $R = 0$, in this paper we have restricted attention to spherical symmetry. The generalisation beyond spherical symmetry and/or to higher dimensions is conceptually straightforward, and will be given elsewhere. As an example in spherical symmetry that is also of interest in its own right, we have implemented the spherical Einstein-Maxwell-charged scalar system. We allow for initial data either on a single outgoing null cone $u = 0$ emerging from a regular centre $R = 0$, or on two intersecting null cones $u = u_0$ and $v = v_0$.

In both setups we have shown second-order self-convergence in all three formulations and second-order convergence between all three formulations. With a regular centre, the convergence is pointwise except near the centre, where it still holds in any function norm. The fact that even the fe formulation converges without any tweaks at the centre came as a pleasant surprise. With the left boundary an ingoing null cone, the convergence is perfectly pointwise everywhere.

As a physics testbed of collapse with data on an outgoing null cone, we have investigated spherical type-II critical collapse of a charged scalar field. This had previously been investigated theoretically in [27], and numerically in [13, 28], but here we have presented the first accurate plots of the universal fine structure in the mass and charge scaling laws. We have also presented some initial evidence for non-universality of the charge scaling fine-structure.

As testbeds for the setup with initial data on two intersecting null cones, we have simulated gravitational collapse with a Minkowski interior, the exact Schwarzschild and extreme Reissner-Nordström solutions (which are non-trivial in our gauge), and extreme Reissner-Nordström perturbed by a complex scalar field on either $u = u_0$ or $v = v_0$.

We plan a study of the solution space of the spherical Einstein-Maxwell-charged scalar system, and in particular an investigation of the “extremal critical collapse conjecture” for the spherical Einstein-charged scalar system [3], see also [2]. We anticipate that both types of numerical domain will be required for this investigation.

Appendix A: The Reissner-Nordström metric in null coordinates

This Appendix presents the RN solution in our variables and gauge choice. In Schwarzschild coordinates, where $R = r$ is a coordinate, the RN metric is

$$ds^2 = -f dt^2 + f^{-1} dr^2 + r^2 d\Omega^2, \quad (\text{A1})$$

where

$$f(r) := 1 - \frac{2\mathcal{M}_0}{r} + \frac{Q_0^2}{r^2}, \quad (\text{A2})$$

and the real constants $\mathcal{M}_0 > 0$ and Q_0 are the usual mass and charge parameters of the RN metric, normalised such that $|Q_0| = \mathcal{M}_0$ represents an extremal black hole. Our dynamical variables \mathcal{M} and Q take the constant values $\mathcal{M} = \mathcal{M}_0$ and $Q = Q_0$. The event and Cauchy horizon are at

$$r_{\pm} = \mathcal{M} \pm \sqrt{\mathcal{M}^2 - Q^2}. \quad (\text{A3})$$

By definition the Hawking mass obeys $r = 2M$ on the event horizon. $M = r_+/2$ at the event horizon is also the irreducible mass of the black hole. In the special case of an extremal black hole, $r_+ = r_- = 2M = \mathcal{M} = Q$.

The tortoise radius r_* is defined, up to addition of a constant, by

$$\frac{dr_*}{dr} := \frac{1}{f(r)}. \quad (\text{A4})$$

With the outgoing and ingoing Eddington-Finkelstein coordinates defined as

$$\bar{u} := t - r_*, \quad \bar{v} := t + r_*, \quad (\text{A5})$$

the metric in the exterior becomes

$$ds^2 = -f d\bar{u} d\bar{v} + r^2 d\Omega^2 \quad (\text{A6})$$

$$= -f d\bar{u}^2 - 2d\bar{u} dr + r^2 d\Omega^2 \quad (\text{A7})$$

$$= -f d\bar{v}^2 + 2d\bar{v} dr + r^2 d\Omega^2. \quad (\text{A8})$$

(Both \bar{v} and \bar{u} increase to the future. In the interior, we define $\bar{u} := r_* - t$ instead to achieve this.)

Writing (A7) in our notation, and choosing our coordinate x to coincide with r , the RN metric in Bondi gauge has the metric coefficients

$$R = x, \quad (\text{A9})$$

$$G = 1, \quad (\text{A10})$$

$$B = \frac{1}{2} \left(1 - \frac{2\mathcal{M}_0}{x} + \frac{Q_0^2}{x^2} \right). \quad (\text{A11})$$

In the double-null coordinates $u = \bar{u}$, $x = \bar{v}$ we have

$$R = r \left(\frac{\bar{v} - \bar{u}}{2} \right), \quad (\text{A12})$$

$$\bar{G} = \frac{1}{2} f(R), \quad (\text{A13})$$

$$B = 0, \quad (\text{A14})$$

where $r(r_*)$ is defined as the function inverse of $r_*(r)$, and \bar{G} denotes the value of G in the particular double-null coordinates \bar{u} , \bar{v} .

If, for given constants \bar{u}_0 , \bar{v}_0 , u_0 , v_0 , we now define the alternative double-null coordinates

$$u(\bar{u}) := u_0 - a \left(r \left(\frac{\bar{v}_0 - \bar{u}}{2} \right) - r_0 \right), \quad (\text{A15})$$

$$v(\bar{v}) := v_0 + b \left(r \left(\frac{\bar{v} - \bar{u}_0}{2} \right) - r_0 \right), \quad (\text{A16})$$

where

$$r_0 := r \left(\frac{\bar{v}_0 - \bar{u}_0}{2} \right), \quad (\text{A17})$$

we have $u(\bar{u}_0) = u_0$, $v(\bar{v}_0) = v_0$, $R_{,u}(u, v_0) = R_{,u*} := -1/a$ and $R_{,v}(u_0, v) = (R_{,v})_* := 1/b$. Inverting (A15,A16), we obtain

$$\bar{u}(u) = \bar{v}_0 - 2r_* \left(r_0 + \frac{u - u_0}{-a} \right), \quad (\text{A18})$$

$$\bar{v}(v) = \bar{u}_0 + 2r_* \left(r_0 + \frac{v - v_0}{b} \right), \quad (\text{A19})$$

$$\begin{aligned} R(u, v) = & r \left[r_* \left(r_0 + \frac{v - v_0}{b} \right) \right. \\ & \left. + r_* \left(r_0 + \frac{u - u_0}{-a} \right) - r_*(r_0) \right]. \end{aligned} \quad (\text{A20})$$

We have

$$\frac{du}{d\bar{u}} = a \bar{G}(\bar{u}, \bar{v}_0), \quad (\text{A21})$$

$$\frac{dv}{d\bar{v}} = b \bar{G}(\bar{u}_0, \bar{v}), \quad (\text{A22})$$

and therefore

$$G(u, v) = \frac{\bar{G}(\bar{v}, \bar{u})}{ab \bar{G}(\bar{v}_0, \bar{u}) \bar{G}(\bar{v}, \bar{u}_0)}, \quad (\text{A23})$$

and hence $G(u_0, v) = G(u, v_0) = G_*$, where

$$G_* := \frac{1}{ab \bar{G}(\bar{u}_0, \bar{v}_0)}. \quad (\text{A24})$$

This is, in implicit form, the exterior metric of RN in the coordinates we use in our null-rectangle tests.

Appendix B: Regular centre

The Minkowski metric in Bondi coordinates, with U the retarded time normalised to be proper time at the centre, is

$$ds^2 = -dU^2 - 2dU dR + R^2 d\Omega^2. \quad (\text{B1})$$

Now let $U = U(u)$ and $R = R(u, x)$. Our metric coefficients become

$$G = U' R_{,x}, \quad (\text{B2})$$

$$B = \frac{U'^2 + 2U' R_{,u}}{2U' R_{,x}}, \quad (\text{B3})$$

$$\Xi R = -\frac{U'}{2}, \quad (\text{B4})$$

$$\mathcal{H} = -\frac{U''}{U'}. \quad (\text{B5})$$

We impose $R(u, 0) = 0$, thus fixing the regular centre at $x = 0$, and we make u proper time at the centre by setting $U = u$. This gives us

$$G(u, 0) = R_{,x}(u, 0), \quad (\text{B6})$$

$$B(u, 0) = \frac{1}{2R_{,x}(u, 0)}, \quad (\text{B7})$$

$$\Xi R(u, 0) = -\frac{1}{2}, \quad (\text{B8})$$

$$\mathcal{H}(u, 0) = 0. \quad (\text{B9})$$

From elementary flatness, these conditions at the centre must also hold in an arbitrary curved spherical spacetime with a regular centre $R = x = 0$ and u proper time at the centre. Beyond spherical symmetry, in spherical coordinates, they will also hold at the regular worldline $R = x = 0$ as long as it is geodesic, see Appendix III.E.2 of Paper I.

Appendix C: Expansions at the centre

For finding G by integration, given R , we need

$$\begin{aligned} \ln \left(\frac{G}{R_{,x}} \right) = & 2\pi(\psi_{(1)}^2 + \chi_{(1)}^2)x^2 \\ & + \frac{4\pi}{3} \left[4(\psi_{(1)}\psi_{(2)} + \chi_{(1)}\chi_{(2)}) \right. \\ & \left. - \frac{R_{(2)}}{R_{(1)}}(\psi_{(1)}^2 + \psi_{(2)}^2) \right] x^3 \\ & + O(x^4). \end{aligned} \quad (\text{C1})$$

Equivalently, for finding R by solving a system of two first-order ODEs, given G , we require

$$\begin{aligned} R = & G_{(0)}x + \frac{G_{(1)}}{2}x^2 \\ & + \frac{1}{3} \left(G_{(2)} - 2G_{(0)}\pi(\psi_{(1)}^2 + \chi_{(1)}^2) \right) x^3 + O(x^4), \end{aligned} \quad (\text{C2})$$

$$\begin{aligned} V = & 1 - 2\pi(\psi_{(1)}^2 + \chi_{(1)}^2)x^2 \\ & + \frac{2\pi}{3G_{(0)}} \left[G_{(1)}(\psi_{(1)}^2 + \chi_{(1)}^2) \right. \\ & \left. - 8G_{(0)}(\psi_{(1)}\psi_{(2)} + \chi_{(1)}\chi_{(2)}) \right] x^3 + O(x^4). \end{aligned} \quad (\text{C3})$$

Note that, given the definition of $V := R_{,x}/G$, to be consistent we should truncate the expansion of V at one order lower in x than that of R , but here we have written out all expansion coefficients that we know in full given a quadratic fit to the evolved quantities. We note in passing that the reverse of (C2) is

$$\begin{aligned} G = & R_{(1)} + 2R_{(2)}x + \left(3R_3 + 2\pi R_{(1)}(\psi_{(1)}^2 + \chi_{(1)}^2) \right) x^2 \\ & + O(x^3). \end{aligned} \quad (\text{C4})$$

We next have

$$\begin{aligned} \frac{Q}{4\pi q} = & \frac{R_{(1)}^2}{3}(\chi_{(1)}\psi_{(0)} - \psi_{(1)}\chi_{(0)})x^3 \\ & + \frac{R_{(1)}}{2} \left[R_{(2)}(\psi_{(0)}\chi_{(1)} - \chi_{(0)}\psi_{(1)}) \right. \\ & \left. + R_{(1)}(\psi_{(0)}\chi_{(2)} - \chi_{(0)}\psi_{(2)}) \right] x^4 \\ & + O(x^5), \end{aligned} \quad (\text{C5})$$

$$\begin{aligned} \frac{A}{4\pi q} = & \frac{R_{(1)}}{6}(\chi_{(1)}\psi_{(0)} - \psi_{(1)}\chi_{(0)})x^2 \\ & + \frac{1}{6} \left[R_{(2)}(\psi_{(0)}\chi_{(1)} - \chi_{(0)}\psi_{(1)}) \right. \\ & \left. + R_{(1)}(\psi_{(0)}\chi_{(2)} - \chi_{(0)}\psi_{(2)}) \right] x^3 \\ & + O(x^4). \end{aligned} \quad (\text{C6})$$

Note that $R_{(3)}$ (or $G_{(2)}$) does not appear to this order.

The expansion of ΞR is

$$\begin{aligned}\Xi R = & -\frac{1}{2} - \frac{\pi}{3}(\psi_{(1)}^2 + \chi_{(1)}^2)x^2 \\ & - \frac{2\pi}{3}(\psi_{(1)}\psi_{(2)} + \chi_{(1)}\chi_{(2)})x^3 + O(x^4),\end{aligned}\quad (\text{C7})$$

where we have already used the expansion of either R or G above, but the expansion of $R\Xi R$ takes the simpler form

$$R\Xi R = -\frac{G_{(0)}}{2}x - \frac{G_{(1)}}{4}x^2 - \frac{G_{(2)}}{6}x^3 + O(x^4), \quad (\text{C8})$$

The two are of course equivalent for analytic functions, but we use the latter in the code.

As one would expect, we can expand $R\hat{\Xi}\psi$ to one order higher than $\hat{\Xi}\psi$, and similarly for $\hat{\Xi}\chi$. The latter expansion is simpler, and is

$$R\hat{\Xi}\psi = \frac{\psi_{(1)}}{2}x + \frac{\psi_{(2)}}{2}x^2 + O(x^3), \quad (\text{C9})$$

$$R\hat{\Xi}\chi = \frac{\chi_{(1)}}{2}x + \frac{\chi_{(2)}}{2}x^2 + O(x^3). \quad (\text{C10})$$

Again none of the expansion coefficients for R (or G) appear to this order.

Finally, we have

$$\begin{aligned}\mathcal{H} = & \frac{8\pi}{3R_{(1)}}(\psi_{(1)}^2 + \chi_{(1)}^2)x \\ & - \frac{4\pi}{3}\left[\frac{R_{(2)}}{R_{(1)}^2}(\psi_{(1)}^2 + \chi_{(1)}^2)\right. \\ & \left.- \frac{3}{R_{(1)}}(\psi_{(1)}\psi_{(2)} + \chi_{(1)}\chi_{(2)})\right]x^2 \\ & + O(x^3).\end{aligned}\quad (\text{C11})$$

Appendix D: Radial null geodesics peeling off the horizon

We consider radial null geodesics in the RN metric. From (A4) and (A5) we have

$$r_{,\bar{v}}(\bar{u}, \bar{v}) = \frac{1}{2}f(r). \quad (\text{D1})$$

Linearising about the event horizon $r = r_+$, we have

$$r_{,\bar{v}} \simeq \kappa(r - r_+), \quad \kappa := \frac{1}{2}f'(r_+), \quad (\text{D2})$$

where κ is the surface gravity. In the subextremal case $\kappa > 0$ the surfaces of constant u , and hence the outgoing radial null geodesics that generate them, peel off the event horizon exponentially. For an arbitrary \bar{v}_0 , we define $\hat{u}(\bar{u})$ by $\hat{u}(\bar{u}) := r(\bar{u}, \bar{v}_0) - r_+$, so that the solution of (D2) can be written as

$$r(\hat{u}, \bar{v}) \simeq r_+ + \hat{u}e^{\kappa(\bar{v} - \bar{v}_0)}. \quad (\text{D3})$$

Note that the coordinate \bar{u} in the metric (A7) diverges at the horizon, but by construction \hat{u} is regular.

A neighbourhood of the event horizon in asymptotically flat charged collapse at sufficiently late time (large \bar{v}) will be approximated by the event horizon in RN. As both \hat{u} and our numerical coordinate u are regular through the horizon, to leading order we must have $\hat{u} \simeq \hat{c}(u - u_h)$ for some constant $\hat{c} > 0$, where the horizon is at $u = u_h$. Differentiating (D3) with respect to u , we find

$$\Xi R \simeq c u e^{\kappa \bar{v}} \quad (\text{D4})$$

near the horizon at late times, where c absorbs \hat{c} and \bar{v}_0 .

We have so far defined \bar{v} only on RN, not on the collapse spacetime that we are trying to model. We note that on RN \bar{v} obeys $\bar{v} = \bar{u} + 2R$. If we assume that for sufficiently early u and sufficiently late \bar{v} the collapse spacetime is approximated by the RN exterior, we can define $\bar{v} = 2R$ on $u = 0$ and propagate it with $\Xi \bar{v} = 0$.

Appendix E: Boundary conditions on an ingoing null cone intersecting an outgoing one

We want to impose consistent null data on $x = 0$, $u > 0$ (the left boundary) and $u = 0$, $x > 0$ (the right boundary), intersecting at the point $u = x = 0$ (the corner). On the left boundary we choose the gauge $B = 0$ ($x = 0$ is null) and $G_{,x} = 0$ (u is an affine parameter), and the electromagnetic gauge $A = 0$. Then $\Xi = \partial_u$ and $\mathcal{H} = 0$ there. In the following, we write $R(u, 0) =: R_l(u)$ and $dR_l/du =: \dot{R}_l(u)$, and similarly for all other quantities on the left boundary.

The ingoing Raychaudhuri equation (48) with $A = B = \mathcal{H} = 0$ gives

$$\ddot{R}_l + 4\pi(\dot{\psi}_l^2 + \dot{\chi}_l^2)R_l = 0. \quad (\text{E1})$$

Note that $\ddot{R}_l \leq 0$, so if $\dot{R}_{l*} < 0$ at the corner (as we shall always assume), then $\dot{R}_l < 0$ for all $u \geq 0$. Eq. (28) with $A = B = 0$ gives

$$\dot{Q}_l = 4\pi q R_l^2(\chi_l \dot{\psi}_l - \psi_l \dot{\chi}_l), \quad (\text{E2})$$

and Eq. (33) with $B = 0$ gives

$$\frac{2\dot{R}_l R_{,xl}}{G_l} = C_l - 1, \quad (\text{E3})$$

where $R_{,xl}(u) := R_{,x}(u, 0)$ and C_l is used as a shorthand for

$$C_l := \frac{2}{R_l} \left(\mathcal{M}_l - \frac{Q_l^2}{2R_l} \right), \quad (\text{E4})$$

compare the definitions (31) and (36). With $A = B = 0$, and using (E3) to eliminate $R_{,xl}$, (38) becomes

$$\begin{aligned}\dot{\mathcal{M}}_l = & -2\pi \frac{R_l^2}{\dot{R}_l} (C_l - 1)(\dot{\psi}_l^2 + \dot{\chi}_l^2) \\ & + 4\pi q Q_l R_l (\chi_l \dot{\psi}_l - \psi_l \dot{\chi}_l).\end{aligned}\quad (\text{E5})$$

Note that $\dot{\mathcal{M}}_l$ can have either sign. Complete boundary data are now obtained as follows.

1) We fix the physical corner data R_* , \mathcal{M}_* and Q_* and define C_* from them by (E4). We fix two of the three gauge-dependent corner values G_* , \dot{R}_{l*} and $R_{,x*}$, with the third one given by the constraint

$$\frac{2\dot{R}_{l*}R_{,x*}}{G_*} = C_* - 1. \quad (\text{E6})$$

2) We fix the gauge on the right boundary $u = 0$ by either setting $G(x, 0) = G_*$ (affine initial gauge) or $R(x, 0) = R_* + R_{,x*}x$ (Bondi initial gauge). We fix the gauge on the left boundary by setting $G_l(u) = G_*$ (affine left gauge). We now fix scalar field data $\psi_l(u)$, $\chi_l(u)$ on the left boundary and $\psi(0, x)$, $\chi(0, x)$ on the right boundary.

For the solution to be sufficiently often differentiable in a neighbourhood of the corner, we need to impose a sufficient number of corner conditions on the derivatives of the boundary data. Here we avoid this complication by assuming that the scalar field data are bounded away from the corner.

3) We solve (E1) as a second-order linear ODE for R_l , starting from R_* and \dot{R}_{l*} , then (E2) as a first-order ODE for Q_l , starting from Q_* , and finally (E5) as a first-order ODE for \mathcal{M}_l , starting from \mathcal{M}_* .

4) From (E3) we read off

$$V_l = \frac{C_l - 1}{2\dot{R}_l}. \quad (\text{E7})$$

We now have the data that we need to start up the integration of the hierarchy equations at $x = 0$, namely $Q = Q_l$ for (27), $A = 0$ for (30), either $R = R_l$ and $V = V_l$ for (65,64) or $G = G_*$ for (39), $\Xi R = \dot{R}_l$ for (42), $\hat{\Xi}\psi = \dot{\psi}_l$ for (43), $\hat{\Xi}\chi = \dot{\chi}_l$ for (44), and $\mathcal{H} = 0$ for (45).

In the simple case where $\psi_l = \chi_l = 0$ the boundary ODE system becomes trivial, giving $Q_l = Q_*$, $\mathcal{M}_l = \mathcal{M}_*$, and $R_l = R_* + \dot{R}_{l*}u$.

Appendix F: Discretization of the left boundary equations

In the continuum, the data on $x = 0$ are automatically compatible with the evolution equations for ψ , χ and R and/or G on $x \geq 0$. To make the discretised versions compatible as well, rather than ψ_l and χ_l we specify $\dot{\psi}_l$ and $\dot{\chi}_l$, together with corner values ψ_* and χ_* . We write (40) in first-order form, and use the same ODE solver that we use to evolve ψ , χ and R and/or G in u in the bulk to also evolve Q_l ,

\mathcal{M}_l , \dot{R}_l , R_l , ψ_l and χ_l on the left boundary. With $A = B = 0$ on the left boundary, the values of $\psi_{,u}$, $\chi_{,u}$, $R_{,u}$ and/or $(\ln G)_{,u} = 0$ are then the same, up to round-off error, in the boundary ODE system and at $x = 0$ in the bulk PDE system.

The Runge-Kutta ODE solver that we use for the time integration assumes that the ODE system is autonomous. We add u as an evolved variable to the set of left-boundary variables, in order to access the given functions $\psi_l(u)$ and $\dot{\chi}_l(u)$ at the correct substep values of u .

Appendix G: Convergence testing

For any computed variable f , we define

$$\mathcal{E}[f](u, x; h) := \left(\frac{h}{h_{\text{ref}}} \right)^{-2} (f(u, x; h) - f(u, x; h/2)) \quad (\text{G1})$$

where $h := \Delta x = x_{\text{max}}/N_x$, and we assume Δu is proportional to h . For a numerical quantity at resolution h , given that our numerical methods are designed to be second-order accurate, we expect the Richardson expansion

$$f(u, x; h) = f_0(u, x) + h^2 f_2(u, x) + h^3 f_3(u, x) + O(h^4) \quad (\text{G2})$$

to hold, where $f_0(u, x)$ is the (unknown) continuum solution and $f_i(u, x)$ are (discretisation-dependent, unknown) error terms, and hence

$$\mathcal{E}[f](u, x; h) = h_{\text{ref}}^2 \left(\frac{3}{4} f_2(u, x) + \frac{7}{8} h f_3(u, x) + O(h^2) \right). \quad (\text{G3})$$

Hence if $\mathcal{E}[f](u, x; h)$ for different h are almost equal, we see pointwise second-order convergence, in the sense that the numerical error is dominated by the term $h^2 f_2$. $\mathcal{E}[f](u, x; h)$ evaluated at any h then provides an estimate of the actual error at the reference resolution $h = h_{\text{ref}}$.

We can also test the convergence (to zero) of $f := M - \tilde{M}$, or of the difference f of any variable computed in two different formulations. We then plot

$$\mathcal{E}[f](u, x; h) := \left(\frac{h}{h_{\text{ref}}} \right)^{-2} f(u, x; h), \quad (\text{G4})$$

which, as $f_0(u, x) = 0$, we expect to take values

$$\mathcal{E}[f](u, x; h) = h_{\text{ref}}^2 (f_2(u, x) + h f_3(u, x) + O(h^2)). \quad (\text{G5})$$

[1] C. Gundlach, D. Hilditch and T. W. Baumgarte, Simulations of gravitational collapse in null coordinates: I. Formulation and weak field tests in Bondi-like gauges, *Phys. Rev. D* **110**, 024018 (2024), [arXiv:2404.15105](https://arxiv.org/abs/2404.15105).

[2] C. Kehle and R. Unger, Gravitational collapse to extremal black holes and the third law of black hole thermodynamics, *J. Eur. Math. Soc.* (2025), published on line first, [arXiv:2211.15742](https://arxiv.org/abs/2211.15742).

[3] C. Kehle and R. Unger, Extremal black hole formation as a critical phenomenon, [arXiv:2402.10190](https://arxiv.org/abs/2402.10190).

[4] C. Gundlach, T. W. Baumgarte and D. Hilditch, Simulations of gravitational collapse in null coordinates: II. Critical collapse of an axisymmetric scalar field, *Phys. Rev. D* **110**, 024019 (2024), [arXiv:2404.15839](https://arxiv.org/abs/2404.15839).

[5] R. S. Hamade and J. M. Stewart, The spherically sym-

metric collapse of a massless scalar field, *Class. Quant. Grav.* **13**, 497 (1996), [gr-qc/9506044](#).

[6] M. L. Gnedin and N. Y. Gnedin, Destruction of the Cauchy horizon in the Reissner-Nordstrom black hole *Class. Quant. Grav.* **10**, 1083 (1993).

[7] L. M. Burko and A. Ori, Late-time evolution of non-linear gravitational collapse, *Phys. Rev. D* **56**, 7820 (1997), [gr-qc/9703067](#).

[8] K. Murata, H. Reall and N. Tanahashi, What happens at the horizon(s) of an extreme black hole?, *Class. Quantum Grav.* **30**, 235007 (2013) [arXiv:1307.6800](#).

[9] D. Garfinkle, Choptuik scaling in null coordinates, *Phys. Rev. D* **51**, 5558 (1995), [gr-qc/9412008](#).

[10] C. Gundlach, T. W. Baumgarte and D. Hilditch, Critical phenomena in gravitational collapse with two competing massless matter fields, *Phys. Rev. D* **100**, 104010 (2019), [arXiv:1908.05971](#).

[11] D. S. Goldwirth and T. Piran, Gravitational collapse of massless scalar field and cosmic censorship, *Phys. Rev. D* **36**, 3575 (1987).

[12] C. Gundlach, R. Price and J. Pullin, Late-time behavior of stellar collapse and explosions: II. Non-linear evolution, *Phys. Rev. D* **49**, 890 (1994), [gr-qc/9307010](#).

[13] S. Hod and T. Piran, Critical behaviour and universality in gravitational collapse of a charged scalar field, *Phys. Rev. D* **55**, 3485 (1997), [gr-qc/9606093](#).

[14] M. Pürer, S. Husa and P. C. Aichelburg, News from critical collapse: Bondi mass, tails, and quasinormal modes, *Phys. Rev. D* **71**, 104005 (2005), [gr-qc/0411078](#).

[15] P. R. Brady and J. D. Smith, Black hole singularities: a numerical approach, *Phys. Rev. Lett.* **75**, 1256 (1995), [gr-qc/9506067](#).

[16] R. Gómez, P. Papadopoulos, and J. Winicour, Null cone evolution of axisymmetric vacuum spacetimes, *J. Math. Phys.* **35**, 4184 (1994), [gr-qc/0006081](#).

[17] C. Reisswig, N. T. Bishop and D. Pollney, General relativistic null-cone evolutions with a high-order scheme, *Gen. Rel. Gravit.* **45**, 1069 (2013), [arXiv:1208.3891](#).

[18] J. Winicour, Characteristic evolution and matching, *Living Rev. Relativ.* **8**, 10 (2005).

[19] J. A. Crespo, H. P. de Oliveira and J. Winicour, The affine-null formulation of the gravitational equations: spherical case, *Phys. Rev. D* **100**, 104017 (2019), [arXiv:1910.03439](#).

[20] T. Mädler, O. Baake, H. Hosseini, J. Winicour, Apparent horizon tracking in supercritical solutions of the Einstein-scalar field equations in spherical symmetry in affine-null coordinates, *Phys. Rev. D* **110**, 044061 (2024), [arXiv:2405.19122](#).

[21] P. M. Chesler and L. G. Yaffe, Holography and colliding gravitational shock waves in asymptotically AdS5 spacetime, *Phys. Rev. Lett.* **106**, 021601 (2011), [arXiv:1011.3562](#).

[22] P. M. Chesler and L. G. Yaffe, Numerical solution of gravitational dynamics in asymptotically anti-de Sitter spacetimes, *JHEP* **2014**, 86 (2014), [arXiv:1309.1439](#).

[23] P. M. Chesler and D. A. Lowe, Nonlinear evolution of the AdS₄ black hole bomb, *Rev. Lett.* **122**, 181101 (2019), [arXiv:1801.09711](#).

[24] P. M. Chesler, Hairy black resonators and the AdS₄ superradiant instability, *Phys. Rev. D* **105**, 024026 (2022), [arXiv:2109.06901](#).

[25] J. Winicour, The affine-null metric formulation of the gravitational equations, *Phys. Rev. D* **87**, 124027 (2013), [arXiv:1303.6969](#).

[26] B. Porto-Veronese and C. Gundlach, Critical phenomena in gravitational collapse with competing scalar field and gravitational waves in 4+1 dimensions, *Phys. Rev. D* **106**, 104044 (2022), [arXiv:2209.08404](#).

[27] C. Gundlach and J. M. Martín-García, Charge scaling and universality in critical collapse, *Phys. Rev. D* **54**, 7353 (1996), [gr-qc/9606072](#).

[28] R. J. W. Petryk, Maxwell-Klein-Gordon Fields in Black Hole Spacetimes, Ph.D. thesis, The University of British Columbia, Vancouver (2005), accessed on <https://laplace.physics.ubc.ca/People/matt/Doc/Theses>.

[29] C. Gundlach and T. W. Baumgarte, Critical gravitational collapse with angular momentum. II. Soft equations of state, *Phys. Rev. D* **97**, 064006 (2018), [arXiv:1712.05741](#).

[30] O. Baake and O. Rinne, Superradiance of a charged scalar field coupled to the Einstein-Maxwell equations, *Phys. Rev. D* **94**, 124016 (2016), [arXiv:1610.08352](#).

[31] Z. Gelles and F. Pretorius, Accumulation of charge on an extremal black hole's event horizon, [arXiv:2503.04881](#).